IEEE Access
Multidisciplinary | Rapid Review | Open Access Journal

Received 10 July 2022, accepted 20 July 2022, date of publication 1 August 2022, date of current version 15 August 2022.

Digital Object Identifier 10.1109/ACCESS.2022.3195940

RESEARCH ARTICLE

Battery Energy Management Techniques for an Electric Vehicle Traction System

AHMED SAYED ABDELAAL, SHAYOK MUKHOPADHYAY, (Member, IEEE), AND HABIBUR REHMAN, (Member, IEEE)

Department of Electrical Engineering, American University of Sharjah, Sharjah, United Arab Emirates

Corresponding author: Shayok Mukhopadhyay (smukhopadhyay@aus.edu)

This work was supported in part by the Open Access Program from the American University of Sharjah, and in part by the Faculty Research Grant FRG20-M-E95.

ABSTRACT This paper presents two battery energy management (BEM) techniques for an electric vehicle (EV) traction system which incorporates an indirect field-oriented (IFO) induction motor (IM) drive system. The main objective of the proposed BEM techniques is to regulate the IM's speed while minimizing the lithium-ion (Li-ion) battery bank state of charge (SOC) reduction and state of health (SOH) degradation. In contrast to most of the existing work, the proposed BEM techniques operate without any prior knowledge of driving profiles or road information. The first BEM technique incorporates two cascaded fuzzy logic controllers (CSFLC). In CSFLC, the first fuzzy logic controller (FLC) generates the reference current signal for regulating the motor speed, while the second FLC generates a variable gain that limits the current signal variation based on the battery SOC. The second BEM technique is based on model predictive control (MPC) which generates the current signal for the speed regulation. However, this work introduces a new way of tuning the MPC input weight using battery information. It features a fuzzy tuned model predictive controller (FMPC), where an FLC adjusts the input weight in the MPC objective function such that the battery SOC is considered while generating the command current signal. Furthermore, this work utilizes a model-in-loop strategy comprising a Chen and Mora (CM) battery model and the experimentally obtained battery bank power consumption to estimate the increase in battery bank runtime and lifetime. A real-time implementation is carried out on a prototype EV traction system using the New European Drive Cycle (NEDC) and the Supplemental Federal Test Procedure (US06) drive cycles. The experimental results validate that the proposed CSFLC and FMPC BEM techniques exhibit a lower reduction in the battery SOC and SOH degradation, thus prolonging the battery bank runtime and lifetime as compared to the conventional FLC and MPC speed regulators. Further experimentation demonstrates the superiority of the FMPC technique over the CSFLC technique due to the lesser computational burden and higher average energy saving.

INDEX TERMS Battery energy management, electric vehicle traction system, field oriented control, model predictive control, fuzzy logic control, fuzzy weight tuning, state of charge, state of health.

I. INTRODUCTION

A major consequence of fossil fuel consumption is environmental pollution, which can be attributed to emissions by the transportation industry [1]. Numbers from the Intergovernmental Panel on Climate Change ascribe nearly 14% of greenhouse gas emissions as a direct result of fossil fuel consumption by the transportation industry [1]. Consequently, there has been an emphasis on a shift toward cleaner sources of energy in this sector. Battery powered electric vehicles (BEV) have been an attractive alternative for several reasons ranging from lower operating and maintenance costs, lack of air pollution, and a lowered dependence on fossil fuels [1], [2]. A significant shortcoming of BEVs is the

The associate editor coordinating the review of this manuscript and approving it for publication was Pinjia Zhang.

limited driving range resulting from the low energy density of batteries found today; 200-300 Wh/L for Lithium-ion (Li-ion) batteries as opposed to 8800 Wh/L for gasoline fuel [3], [4]. To combat these issues, this project presents two battery energy management (BEM) strategies that decrease battery energy consumption and state of charge (SOC) decline, thus lowering battery state of health (SOH) degradation. Furthermore, a model-in-loop strategy is employed to estimate the battery bank runtime and lifetime. The runtime represents the time required to go from 100% SOC to 20% SOC. The battery lifetime is directly related to its SOH [5]. Therefore, it is important to keep track of the battery's SOH because it indicates the maximum releasable battery capacity. For EV applications, a battery reaches its end-of-life (EOL) when its SOH drops by 20% [5], [6]. In other words, a longer runtime means that a vehicle is capable of traveling longer distances before requiring recharging. While a longer lifetime means that the batteries will operate for a longer time before requiring replacement.

The majority of electric vehicle (EV) BEM techniques can be categorized into rule-based strategies and optimization-based strategies [7], [8]. The rule-based strategies involve using rule tables which require development by an experienced user. However, it is difficult for a rule-based strategy to find the optimal solution without intricate design and repetitive iterations to improve the BEV performance [8]. The optimization-based strategies are utilized to obtain optimal or near optimal solutions for the system's objective [9], [10].

Some of the rule-based techniques in the literature involve using a fuzzy logic controller (FLC) in the management of multiple sources such as fuel cells, combustion engines, ultra-capacitors and batteries. An FLC divides the power demand over the multiple sources such that each source operates at its highest efficiency. In the works of [11], [12], an FLC was used to share the power demand with an ultra-capacitor or an engine, such that the load current does not exceed the maximum battery current and to prevent the battery from over discharging. In [13], a super capacitor (SC) is added to an EV traction system to absorb the current discharge stress on the battery due to unplanned situations. The FLC in [13] shifts the abrupt energy demand to an SC to reduce the discharge stress on the battery during the acceleration phase. On the other hand, [14] proposes an adaptive fuzzy controller which shares the energy consumption between a battery and an SC by means of a DC-DC converter. A contour positioning system was used to obtain the road slope information which was used to estimate the energy required to reach the destination. The control algorithm split the energy demand between the battery and the SC such that the battery supplies a constant current while the SC supplies the peak current and absorbs the regenerated current during braking thus reducing the fast charging and discharging effects on the battery. The authors in [15] proposed a predictive protection algorithm that used an FLC to monitor the road information and the SOH of the battery, then produced a signal to charge or discharge the battery. In [16], an FLC is designed which takes into account the SOC of the battery, the input reference speed, and the commanded vehicle acceleration then produced a setpoint for the battery output power. The work in [17] created an intelligent energy management system that monitors the torque signal and the battery SOC then generates the electric throttle signal to regulate the motor speed. Furthermore, [18] introduced a neural FLC to manage regenerative braking in a hybrid EV. The controller monitors the engine speed and power delivered then accurately determines the required torque for the application [18]. Once the delivered power exceeds the required value, the regenerative braking system starts charging the battery bank using the excess power generated by the engine [18]. A common aspect in the literature is the utilization of the FLC's ability to incorporate the user's expertise to dictate the system's operation without requiring an accurate system model [19]. In our case, a cascaded FLC that incorporates the motor speed error, change in speed error, and the battery SOC was developed based on user experience to regulate the motor speed while reducing the energy consumption. Due to the FLC's ability at handling induction motor (IM) drive non-linearities, speed variations, and parameter changes, it is preferred over the conventional PI controller [19]. It is worth noting that the previous events tend to detune the PI controller and degrade its performance with the IM drive [19].

Regarding the use of optimization-based strategies, [20] develops a driving pattern recognition system using artificial neural networks which monitors the driver's behavior and estimates a driving cycle for the specified user. A stochastic predictive model is used in [21] to predict the driving profile of a bus using Markov Chain Monte Carlo methods. Also, in [21] the SOC consumption is optimized using dynamic programming (DP). Furthermore, the neural networks and Markov Chain Monte Carlo methods are dependent on historical data collected from the driving profile of the consumer. An adaptive equivalent consumption minimization strategy (A-ECMS) is introduced in [22], as an upgrade to the original ECMS. The A-ECMS compares the current battery SOC with the desired SOC and generates a new optimal equivalent factor that minimizes the error. The authors in [23] combined historical data of the SOC trajectory and torque demand of a city bus to create a batch iterative learning control algorithm. The algorithm is used in conjunction with an MPC such that the MPC performs its real-time predictive control while exploiting the repetitive nature of the historical data to perform a batch-wise feedback control. The driving velocity profile is obtained using a synthesized velocity profile prediction (SVPP) method and DP is used to calculate the optimal battery SOC constraints at every iteration [24]. In [25], the energy management strategy contained a long short term memory-based (LSTM) velocity predictor. The vehicle load power is obtained by combing information from vehicle velocity with the vehicle parameters. An MPC allocated the load power to an ultra-capacitor and a battery through a DC-DC converter such that the three components operate at maximum efficiency, and the total power dissipation is

minimized. An MPC-based strategy is used to manage the energy consumption using the route information in [26]. The road slope information is loaded into the MPC which accelerated the vehicle in advance such that an abrupt acceleration does not have a substantial impact on the energy consumption.

Furthermore, [27] generates a new reference velocity for the vehicle at different road slopes using the previously obtained road slope information. When a road slope is encountered, the reduction in speed due to the road slope results in the desired vehicle speed. In contrast, the road information is used to generate the optimal battery SOC using DP at different setpoints in [28]. The setpoints are then loaded into an MPC which controls the maximum battery output power such that the battery's SOC follows the optimal SOC at each setpoint. Similarly, [29] created an adaptive energy management strategy for an MPC controlled EV. The MPC follows an SOC reference trajectory which is generated through DP and historical data of the vehicle velocity. Furthermore, the current traffic information is incorporated and processed through deep neural networks which predict the future vehicle velocity then update the SOC reference trajectory. In [30], a nonlinear-MPC combines vehicle-to-vehicle communication and road slope information. This method optimizes the vehicle acceleration such that the battery SOC consumption is minimized. The authors in [31] created a time series model that forecasts the power demand based on the vehicle speed and acceleration, road slope information, brake pedal position, historical power demand, and present power demand. A nonlinear predictive controller determined the optimal power demand over the prediction horizon, while a receding horizon algorithm limited the vehicle's power consumption. In [32], a sequence-based velocity profile predictor is introduced. It identifies the different power losses associated with the hybrid energy storage system and battery capacity due to the changing velocity profile, then formulates and solves a power split cost function through chaotic particle swarm optimization. The work of [33] formulates a power split function involving the battery SOC and the vehicle speed then uses sequential programming to solve the problem. The optimal position for the brake and acceleration pedals is regulated accordingly.

In the preceding optimization-based strategies, DP is used as a benchmark for comparison with the newly developed energy management strategies [1], [8], [25]. However, DP cannot be implemented in real-time due to its high computational cost [25]. Other optimization strategies include the equivalent consumption minimization strategy (ECMS) and convex programming (CP), which are used in conjunction with an MPC to optimize energy saving and reach a near optimal solution. In these strategies, the accuracy is compromised for a lower computational burden, as compared to DP [8]. However, the ECMS strategy requires choosing an optimal equivalent factor which is obtained by solving a two point boundary value problem [8]. The solution to this problem may be difficult to obtain and in some cases impossible [8]. The optimal equivalent factor is usually obtained through rigorous experimentation and may not be effective throughout the entire drive cycle [8]. The CP method can obtain the global optimal solution. However, it requires the representation of the whole system by single or multiple convex functions in addition to the prior knowledge of the drive cycle [8]. Furthermore, the MPC-based energy management strategies revolve around forecasting velocity profiles or driving behaviors, and planning SOC reference trajectories or maximum battery output power before the operation of the vehicle. Consequently, the techniques in [20], [21], [23], [24], [26]–[28], [30]–[32] are dependent upon storing and pre-processing historical data, which has a substantial memory requirement, before initiating the optimization algorithm.

A real-time BEM strategy needs to have a low computational cost and a low memory requirement [23], [34]. Furthermore, the strategy must adapt to varying driving styles and cannot be limited to specific driving profiles or known road information, unlike the techniques in [20], [24], [26]–[28], as this kind of information may be difficult to obtain [27]. Table 1 contains a comparison between the proposed BEM techniques and similar techniques in the literature in terms of road information, computational effort, and type of operation. Due to the difficulty in calculating the battery SOH's instantaneous value, the SOH degradation is often ignored in the literature [5]. Another issue neglected by the MPC-based techniques is the selection of the input weights in the MPC objective function [23], [26], [28], [30]–[32]. At the present, the selection of these weights presents a challenge and there is no clear way of determining their values [35]. Recently, an FLC has been used to tune the MPC objective function weights depending on the d-axis and q-axis current errors to reduce the overall motor torque ripples [36]. Furthermore, a self-tuned FLC is introduced in [37], to improve the transient performance of an IM drive by generating an output scaling factor for the control signal. The primary objective in [37] is to achieve a superior speed performance in terms of overshoot, rise time, settling time, and recovery time. In addition, [38] addresses the effects of the long sampling time required for the execution of the FLC on the performance of the IM drive, and then it introduces a multiple timer strategy to combat these effects. The IM drive was run on a small sampling time so that the motor speed performance is not degraded [38]. On the other hand, the FLC controllers were run on a separate timer with a larger sampling time [38]. The same strategy is adopted, and a comparison between the proposed and conventional techniques is presented in this work. Although an FLC has been used in conjunction with an MPC in the past, and a self-tuned FLC strategy was already proposed, the effects of such uses on reducing SOH degradation or reducing the battery SOC consumption have so far not been addressed. To sum up, the current literature deals with the EV traction system IM drive components as a black box [8]. Since the detailed IM drive system dynamics are not considered in [15]–[18], [22], [30]–[33], this work

TABLE 1. Comparison between the proposed BEM techniques and the existing approaches in the literature.

BEM technique	Road information	Computational effort	Mode of operation
Proposed CSFLC	No	High	Real-time
Proposed FMPC	No	Medium	Real-time
FLC [11], [12]	No	Medium	Real-time
MPC [25], [27]	No	Medium	Real-time
DP [21], [24], [28]	Yes	High	Offline
A-ECMS [8]	Yes	High	Offline
R-EMS [7]	No	High	Real-time
Predictive protection algorithm [15]	Yes	High	Offline

features experimental modifications to an actual EV traction IM drive system powered by a 400 V Li-ion battery bank.

The main contributions of this work are:

1) Two BEM techniques that run in real-time without requiring driving profiles or road information.
2) BEM strategies that manipulate the architecture of the conventional FLC and MPC speed regulators of induction motor-driven EV traction system.
   a) The first technique is based on the cascaded FLC (CSFLC) which comprises a conventional FLC speed regulator and a second variable gain FLC placed in cascade. The second FLC acts as an auto tuner which modifies the torque regulating current signal variations based on the battery bank SOC.
   b) The second technique is the FLC tuned MPC (FMPC) energy management system. An FLC generates the input weight in the cost function of the MPC based on the first and second order derivatives of the battery bank's SOC. The resulting current signal regulates the speed of the IM while conserving the battery energy.
3) A new way of tuning the MPC input weight and FLC output scaling factor using the battery information.
4) The SOH's instantaneous value for the battery bank is estimated, and a model-in-loop strategy is employed using the Chen and Mora (CM) battery model to estimate the number of hours till the EOL of the battery bank.

The remainder of the paper is organized as follows; section II contains the EV traction system components and hardware specifications, section III describes the BEM strategies, section IV shares the experimental results and related discussion followed by the concluding remarks in section V of this paper.

II. EV TRACTION SYSTEM COMPONENTS AND MODELING

A. INDUCTION MOTOR DRIVE

The IM modeled in the synchronously rotating dq-coordinate system can be shown by equations (1) - (6) [39].

$$V_{sd} = R_s i_{sd} + \frac{d\lambda_{sd}}{dt} - \omega_e \lambda_{sq} \tag{1}$$

$$V_{sq} = R_s i_{sq} + \frac{d\lambda_{sq}}{dt} - \omega_e \lambda_{sd} \tag{2}$$

$$V_{rd} = R_r i_{rd} + \frac{d\lambda_{rd}}{dt} - \omega_{sl} \lambda_{rq} \tag{3}$$

$$V_{rq} = R_r i_{rq} + \frac{d\lambda_{rq}}{dt} - \omega_{sl} \lambda_{rd} \tag{4}$$

$$T_{em} = \frac{3p}{2} \frac{L_m}{L_r} (\lambda_{rq} i_{rd} - \lambda_{rd} i_{rq}) \tag{5}$$

$$\frac{d\omega_m}{dt} = \frac{1}{J} (T_{em} - T_L - B\omega_m) \tag{6}$$

where V, i, λ are the dq-components for the stator and rotor voltages, currents and flux respectively. The R_s and R_r terms are the stator and rotor resistances respectively and J, B, T_{em}, T_L are the motor inertia, coefficient of friction, electromagnetic torque, and load torque while, ω_m, ω_e, ω_{sl} represent the mechanical speed, d-axis rotation speed and rotor axis rotational speed. Here ω_e is selected to be equal to the synchronous speed $\omega_{sync} = 2\pi f$ radians per second. Equations (1) - (5) represent the electrical equations and (6) shows the mechanical coupling equation of the induction machine. Equation (7) represents the dq-fluxes as a function of the dq-currents in matrix form.

$$\begin{bmatrix} \lambda_{sd} \\ \lambda_{sq} \\ \lambda_{rd} \\ \lambda_{rq} \end{bmatrix} = \begin{bmatrix} L_s & 0 & L_m & 0 \\ 0 & L_s & 0 & L_m \\ L_m & 0 & L_r & 0 \\ 0 & L_m & 0 & L_r \end{bmatrix} \begin{bmatrix} i_{sd} \\ i_{sq} \\ i_{rd} \\ i_{rq} \end{bmatrix} \tag{7}$$

Applying the principle of indirect field-orientation (IFO) by setting $\lambda_{rq} = 0$, (8) can be derived from (3) and (7) and is used to estimate the rotor flux. Furthermore, (4) can be combined with (7) yielding (9) [39]. Equation (9) is used for calculating the rotor slip.

$$\lambda_{rd} = L_m i_{sd} \tag{8}$$

$$\omega_{sl} = \frac{L_m}{\tau_r} \frac{i_{sq}}{\lambda_{rd}} \tag{9}$$

where τ_r is the rotor time constant.

We can derive the state-space representation of the IFO IM drive by combining (5) and (7) yielding

$$T_{em} = \frac{3p}{2} \frac{L_m}{L_r} (\lambda_{rd} i_{sq}) \tag{10}$$

A relation governing the speed ω_m and the current i_{sq} can be derived by combining (6) and (10).

$$\frac{d\omega_m}{dt} = \frac{1}{J} \left(\frac{3p}{2} \frac{L_m}{L_r} (\lambda_{rd} i_{sq}) - T_L - B\omega_m \right) \tag{11}$$

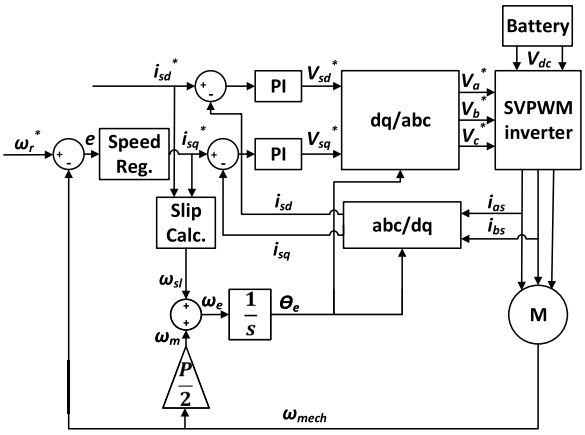

FIGURE 1. Overall EV traction IM drive system.

At a given load T_L, taking the derivative of (11) yields

$$\frac{d^2\omega_m}{dt^2} = -\frac{B}{J}\frac{d\omega_m}{dt} + \frac{3p}{2}\frac{L_m}{L_r}\frac{\lambda_{rd}}{J}\frac{di_{sq}}{dt} \tag{12}$$

The state-space representation of the IFO IM drive is given by (13) and (14) [40], [41].

$$\begin{bmatrix}\ddot{\omega}_m \\ \dot{\omega}_m\end{bmatrix} = \begin{bmatrix}-\frac{B}{J} & 0 \\ 1 & 0\end{bmatrix}\begin{bmatrix}\dot{\omega}_m \\ \omega_m\end{bmatrix} + \begin{bmatrix}\frac{3p}{2}\frac{L_m}{L_r}\frac{\lambda_{rd}}{J} \\ 0\end{bmatrix}\frac{di_{sq}}{dt} \tag{13}$$

$$\omega_m = \begin{bmatrix}0 & 1\end{bmatrix}\begin{bmatrix}\dot{\omega}_m \\ \omega_m\end{bmatrix} \tag{14}$$

The overall EV traction system containing the IFO IM drive and the battery bank is shown in Fig. 1. The slip calculation block performs the rotor flux estimation using (8), then calculates the slip using (9). The d-axis current i_{sd}^* and q-axis current i_{sq}^* regulate the flux and torque of the induction motor respectively. The two inner PI controller loops compare the motor i_{sd} and i_{sq} currents with the reference i_{sd}^* and i_{sq}^* currents and ensure that they are equal during the operation of the EV traction system. The errors produced by the two inner PI controllers are used to generate the reference voltage commands V_{sd}^* and V_{sq}^* respectively. The reference voltages are converted using the dq/abc transformation to V_a^*, V_b^*, and V_c^* reference sinusoidal voltages that are used to generate pulse width modulation (PWM) signals for the inverter. The outer controller loop generates the reference i_{sq}^* torque regulating current signal, and the performance of the MPC, FLC, CSFLC, and FMPC controllers is assessed in this part of the EV traction system. The speed regulator block contains the FLC and MPC speed regulators which will be compared with the CSFLC and FMPC BEM techniques. The final value, I_{sd}, for a step command i_{sd}^*, was obtained by running the IM at its rated voltage and frequency with no load. Whereas, the final value, I_{sq}, for a step command i_{sq}^*, was obtained by running the IM at rated speed and rated voltage with a load. The I_{sd} and I_{sq} current values used in this work are 1 A and 1.5 A respectively. The inner loop PI current regulator for i_{sd}^* was tuned by applying the step command i_{sd}^*, while setting i_{sq}^* to zero. The outer controller upper and lower saturation limits are set to $2I_{sq}$ and $-2I_{sq}$ respectively [42].

TABLE 2. Three-phase inverter switching states.

Switching states	Q_c	Q_b	Q_a
0	0	0	0
1	0	0	1
2	0	1	0
3	0	1	1
4	1	0	0
5	1	0	1
6	1	1	0
7	1	1	1

B. SPACE VECTOR PWM (SVPWM) INVERTER

A simple three-phase inverter is shown in Fig. 2. The first leg contains switches Q_a and $\bar{Q}_a$, the second leg contains switches Q_b and $\bar{Q}_b$, the third leg contains Q_c and $\bar{Q}_c$, and V_d is the DC bus voltage. The switches on the same leg are complementary and cannot be turned on at the same time [39]. The inverter's output voltage vectors are a result of the eight switching states of the inverter. The switching states are presented in Table 2 where 1 represents ON/Closed condition and 0 represents OFF/Open condition.

Furthermore, the voltage vectors resulting from the inverter switching states in Table 2 are denoted by $\vec{v}_{switching\ state}$ (Q_c Q_b Q_a). The inverter's output voltage vectors are $\vec{v}_0(000)$, $\vec{v}_1(001)$, $\vec{v}_2(010)$, $\vec{v}_3(011)$, $\vec{v}_4(100)$, $\vec{v}_5(101)$, $\vec{v}_6(110)$, $\vec{v}_7(111)$ and they are shown in black on the vector diagram in Fig. 3. Since $\vec{v}_0$ and $\vec{v}_7$ are zero in magnitude, they are not visible in Fig. 3. The V_a^*, V_b^*, V_c^* reference sinusoidal voltages produced by the the IM drive, are converted to their vector format $\vec{v}_s^*$ through (15) [39]. The reference voltage vector $\vec{v}_s^*$ is displayed in red on the vector diagram in Fig. 3. The angle θ_s is the angle between $\vec{v}_s^*$ and $\vec{v}_1$. On the other hand, α is the angle between $\vec{v}_s^*$ and the starting vector in the sector in which $\vec{v}_s^*$ lies. The starting vector is the first vector to cross the angle θ_s in the sector where $\vec{v}_s^*$ lies. Since vector $\vec{v}_2$ is the first vector to cross the angle θ_s in sector 3 (the sector where $\vec{v}_s^*$ lies), then the angle α is formed between vectors $\vec{v}_2$ and $\vec{v}_s^*$.

$$\vec{v}_s^* = V_a^* e^{j0} + V_b^* e^{j\frac{2\pi}{3}} + V_c^* e^{j\frac{4\pi}{3}} = \left\|\vec{v}_s^*\right\| e^{j\theta_s} \tag{15}$$

The purpose of displaying $\vec{v}_s^*$ along with the inverter's output voltage vectors is to locate and identify the inverter's output voltage vectors adjacent to $\vec{v}_s^*$. For example, when $\vec{v}_s^*$ is in sector 3, the adjacent inverter output voltage vectors are $\vec{v}_2^*$, $\vec{v}_6^*$, $\vec{v}_0^*$, and $\vec{v}_7^*$. To synthesize the reference voltage vector $\vec{v}_s^*$, a portion of the sampling time is allotted to each inverter output voltage vector. Given the sampling time T_s and variables x, y, z such that $x + y + z = 1$, reference vector $\vec{v}_s^*$ can be produced if the vector $\vec{v}_2^*$ is ON for time xT_s, and vector $\vec{v}_6^*$ is ON for time yT_s. The remainder of the sampling time $zT_s = (1 - x - y)T_s$ is allotted to the zero magnitude vectors $\vec{v}_0$ and $\vec{v}_7$. In other words, reference vector $\vec{v}_s^*$ can be

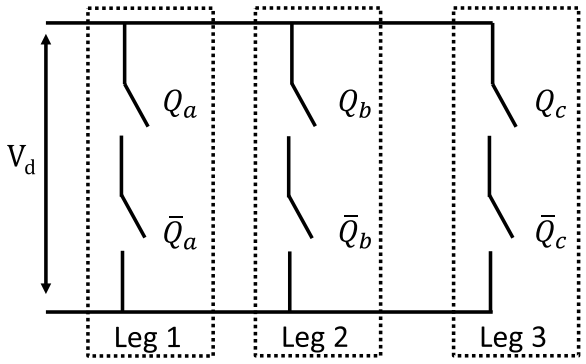

FIGURE 2. Three-phase inverter.

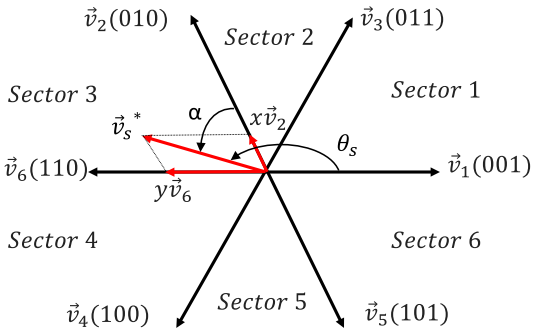

FIGURE 3. Space vector diagram for a three-phase inverter.

represented by (16). Furthermore, (17) - (19) derived in [39] are used to obtain the values for x, y, and z.

$$\vec{v}_s^* = \frac{1}{T_s}[xT_s\vec{v}_2 + yT_s\vec{v}_6 + zT_s \cdot 0] \tag{16}$$

$$x = \frac{2}{\sqrt{3}}\frac{\|\vec{v}_s^*\|}{V_d} sin(60 - \alpha) \tag{17}$$

$$y = \frac{2}{\sqrt{3}}\frac{\|\vec{v}_s^*\|}{V_d} sin(\alpha) \tag{18}$$

$$z = 1 - x - y \tag{19}$$

Finally, the values of x and y can be used to generate the duty cycle for each inverter leg. The inverter leg duty cycle represents the time that an inverter leg produces a voltage V_d. In other words, the upper switch is ON and the lower switch is OFF. For example in leg one, D_a is the time that Q_a spends in ON condition and $\bar{Q}_a$ in OFF condition. Table 3 contains the matrices used to obtain the duty cycles for each inverter leg in all 6 sectors [39]. The overall process is summarized in the flowchart in Fig. 4. Given V_a^*, V_b^*, V_c^* and the DC bus voltage V_d, the reference voltage vector $\vec{v}_s^*$ can be formed using (15). The angle θ_s of the voltage vector $\vec{v}_s^*$ is used to deduce the sector number and the angle α is obtained accordingly. The values of x and y are computed through (17) and (18) using the magnitude of $\vec{v}_s^*$, the angle α and the DC bus voltage V_d. Finally, the inverter leg duty cycles D_a, D_b and D_c are obtained by using x, y, the sector number and Table 3.

TABLE 3. Matrices for obtaining the duty cycle for each inverter leg in the 6 sectors [39].

Sector	Duty cycle
1	$\begin{bmatrix} D_a \\ D_b \\ D_c \end{bmatrix} = \frac{1}{2}\begin{bmatrix} 1 & 1 & 1 \\ 1 & -1 & 1 \\ 1 & -1 & -1 \end{bmatrix} \times \begin{bmatrix} 1 \\ x \\ y \end{bmatrix}$
2	$\begin{bmatrix} D_a \\ D_b \\ D_c \end{bmatrix} = \frac{1}{2}\begin{bmatrix} 1 & 1 & -1 \\ 1 & 1 & 1 \\ 1 & -1 & -1 \end{bmatrix} \times \begin{bmatrix} 1 \\ x \\ y \end{bmatrix}$
3	$\begin{bmatrix} D_a \\ D_b \\ D_c \end{bmatrix} = \frac{1}{2}\begin{bmatrix} 1 & -1 & -1 \\ 1 & 1 & 1 \\ 1 & -1 & 1 \end{bmatrix} \times \begin{bmatrix} 1 \\ x \\ y \end{bmatrix}$
4	$\begin{bmatrix} D_a \\ D_b \\ D_c \end{bmatrix} = \frac{1}{2}\begin{bmatrix} 1 & -1 & -1 \\ 1 & 1 & -1 \\ 1 & 1 & 1 \end{bmatrix} \times \begin{bmatrix} 1 \\ x \\ y \end{bmatrix}$
5	$\begin{bmatrix} D_a \\ D_b \\ D_c \end{bmatrix} = \frac{1}{2}\begin{bmatrix} 1 & -1 & 1 \\ 1 & -1 & -1 \\ 1 & 1 & 1 \end{bmatrix} \times \begin{bmatrix} 1 \\ x \\ y \end{bmatrix}$
6	$\begin{bmatrix} D_a \\ D_b \\ D_c \end{bmatrix} = \frac{1}{2}\begin{bmatrix} 1 & 1 & 1 \\ 1 & -1 & -1 \\ 1 & 1 & -1 \end{bmatrix} \times \begin{bmatrix} 1 \\ x \\ y \end{bmatrix}$

C. AUTOMOTIVE RURAL/URBAN DRIVE CYCLES

Two driving cycles are selected for assessing the BEM technique's energy saving proficiency. A driving cycle comprises data points representing a real life vehicle velocity measured versus time. Drive cycles are commonly used to estimate the fuel consumption and CO_2 emissions of different vehicles for a standardized comparison of vehicle performance. Furthermore, drive cycles have been recently used to compare different EV energy management strategies [7], [8], [23], [24].

The New European Drive Cycle (NEDC) and the Supplemental Federal Test Procedure (US06) drive cycle in Fig. 5 are chosen to compare the BEM techniques in this work. The NEDC drive cycle comprises an urban and extra-urban driving stage. The length of the urban driving cycle is 760 seconds, it starts at second 110 and ends at second 870. The extra-urban driving stage spans a period of 360 seconds starting from second 900 till second 1260. The NEDC drive cycle is a compilation of straight acceleration and constant speed periods and is shown in Fig. 5a. The US06 drive cycle is a

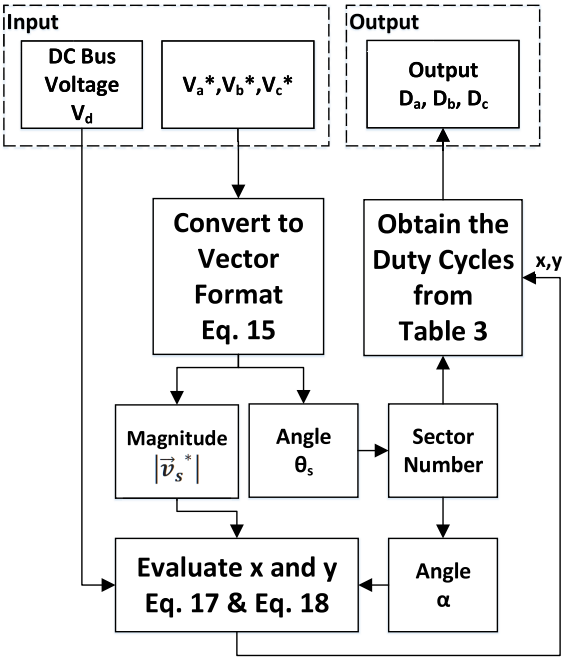

FIGURE 4. Flowchart for the generation of duty cycles for the SVPWM inverter.

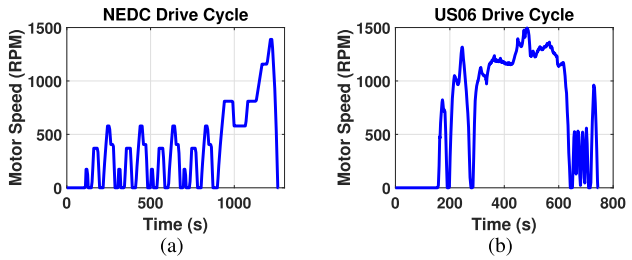

FIGURE 5. (a) NEDC drive cycle, (b) US06 drive cycle.

more aggressive drive cycle as compared to the NEDC drive cycle. It contains high transient accelerations that result in many speed variations, which is typical of on-road driving conditions. The US06 drive cycle starts at second 155 and ends at second 745 with a total duration of 590 seconds. The US06 drive cycle imitates an aggressive driving behavior as shown in Fig. 5b. The speed tracking performance on the NEDC and US06 drive cycles for the FLC, MPC, CSFLC, and FMPC techniques is quantified using the absolute average error given by (20).

$$\text{Absolute average error} = \frac{1}{N}\sum \|e(t)\| \tag{20}$$

where N is the number of samples and $e(t)$ is the motor speed error.

D. LI-ION BATTERY BANK MODEL AND MEASUREMENTS

1) CHEN AND MORA's MODEL

The Chen and Mora (CM) circuit model captures the dynamic characteristics of the battery's terminal voltage, battery parameters variation relative to SOC, and has been the subject

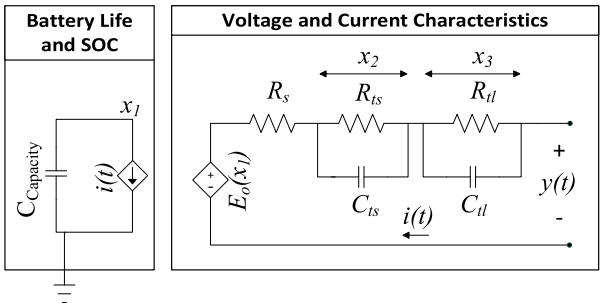

FIGURE 6. Chen and Mora equivalent circuit battery model.

of extensive experimentation in the past decade [43]. Furthermore, the CM model has the ability to incorporate the number of charge/discharge cycles and capacity loss due to self-discharge [43]. These advantages make the CM model an appealing choice for this work. Fig. 6 shows the CM equivalent circuit battery model used in this work. The left half of the circuit shows the battery's SOC dynamics and its behavior in response to a load current. Whereas, the right half of the circuit shows the battery's output voltage with regards to the changing load current. The state x_1 represents the battery's SOC, while x_2 represents the voltage across $R_{ts}||C_{ts}$, and finally, x_3 represents the voltage across $R_{tl}||C_{tl}$. The parallel combination of $R_{ts}||C_{ts}$ represents the short-term terminal voltage dynamics in response to changes in the discharge current. Similarly, the parallel combination $R_{tl}||C_{tl}$ represents the long-term terminal voltage dynamics in response to changes in the discharge current [43]. The CM model is given by (21) - (24) [44].

$$\dot{x}_1(t) = -\frac{1}{C_C}i(t), \quad C_C = 3600Cf_1f_2f_3 \tag{21}$$

$$\dot{x}_2(t) = -\frac{x_2(t)}{R_{ts}(x_1)C_{ts}(x_1)} + \frac{i(t)}{C_{ts}(x_1)} \tag{22}$$

$$\dot{x}_3(t) = -\frac{x_3(t)}{R_{tl}(x_1)C_{tl}(x_1)} + \frac{i(t)}{C_{tl}(x_1)} \tag{23}$$

$$y = E_o(x_1) - x_2(t) - x_3(t) - i(t)R_s(x_1) \tag{24}$$

where the SOC, x_1, is between [0, 1]. The states x_2 and x_3 are non-negative real numbers when the current is flowing out of the battery. The variable C in (21) represents the capacity (A.h) of the battery, while the factors $f_1, f_2, f_3 \in [0, 1]$ in (21) account for the effects of temperature, number of charge and discharge cycles, and self-discharge respectively and they are set to 1 for simplicity. The battery terminal voltage is given by (24) and it is dependent on the states x_2, x_3, the battery current $i(t)$, the series resistance R_s, and the open circuit voltage E_o. The battery parameters E_o, R_{ts}, R_{tl}, C_{ts}, C_{tl} and R_s are given by (25) - (30) [43].

$$E_o(x_1) = -a_1e^{-a_2x_1} + a_3 + a_4x_1 - a_5x_1^2 + a_6x_1^3 \tag{25}$$

$$R_{ts}(x_1) = a_7e^{-a_8x_1} + a_9 \tag{26}$$

$$R_{tl}(x_1) = a_{10}e^{-a_{11}x_1} + a_{12} \tag{27}$$

$$C_{ts}(x_1) = -a_{13}e^{-a_{14}x_1} + a_{15} \tag{28}$$

TABLE 4. Chen and Mora parameters for a 22.2 V, 4 Ah Lithium-Polymer battery [45].

Parameters	Values
a_1	5.112
a_2	40.955
a_3	22.195
a_4	1.9210
a_5	1.759
a_6	3.0435
a_7	0.5505
a_8	30.0475
a_9	0.0551
a_{10}	6.2585
a_{11}	30
a_{12}	0.0551
a_{13}	760.2266
a_{14}	10.7686
a_{15}	685.7457
a_{16}	6036.4
a_{17}	27.5422
a_{18}	3696
a_{19}	0.0439
a_{20}	59.07
a_{21}	0.2246

$$C_{tl}(x_1) = -a_{16}e^{-a_{17}x_1} + a_{18} \tag{29}$$
$$R_s(x_1) = a_{19}e^{-a_{20}x_1} + a_{21} \tag{30}$$

The voltage relaxation test is performed to obtain the open circuit voltage curve for the battery. Next, the curve fitting toolbox is used in MATLAB to obtain the parameters a_1 to a_6 in (25). The remaining Li-ion battery model parameters described by (26) - (29) are obtained by the APE technique. After estimating the battery's parameters a_7 to a_{18} using the APE method, the battery series resistance parameters a_{19}, a_{20} and a_{21} can be obtained from the $R_s(x_1(t))$ vs $x_1(t)$ curve using curve fitting as described in [43]. The battery bank parameters are recorded in Table 4.

2) SOC ESTIMATION

There are several techniques in the literature for computing the battery SOC as presented in [46]. Coulomb counting (CC) is considered one of the conventional techniques and is commonly used in EV literature due to its computational simplicity [46]. A few notable works that compare different energy management strategies and utilize CC to obtain the SOC are [12], [14], [25], [32], [47]–[49]. The mathematical formulation of the CC method is shown in (31).

$$SOC(t) = SOC(t_0) - \frac{1}{C_c}\int_0^t i(t)dt \tag{31}$$

where $SOC(t_0)$ is the initial SOC, C_c is the battery capacity (Ah) and $i(t)$ is the discharge current which is positive while discharging and negative while charging [50]. Therefore, as it can be seen from (31), that the method depends on the accurate measurement of the battery current and estimated initial SOC of the battery [50].

TABLE 5. Parameter B with respect to battery C_{rate}.

Battery C_{rate}	0.5	2	6	10
B	31630	21681	12934	15512

3) SOH ESTIMATION

The SOH is defined as the ratio of the maximum usable capacity to the capacity of a new battery and is represented by (32) [51].

$$\text{SOH} = \frac{C_{max}}{C_c} \times 100\% \tag{32}$$

where C_{max} is the current maximum releasable capacity of the battery and C_c is the capacity of a new battery.

An empirical model for online monitoring of SOH degradation as a function of battery current was developed by [52], [53]. The authors in [52], [53] performed numerous experiments on a Li-ion battery where they investigated the effects of the number of charge/discharge cycles, cycle life, rest time/calendar life, battery temperature, depth of discharge, and discharge rate. Furthermore, [52], [53] share theoretical justifications and derivations for the model. This SOH empirical model is widely adopted in EV literature and is represented by (33) [5], [6], [47], [54].

$$\frac{dSOH}{dt} = \frac{C_{rate} \times C_c \times \left(Be^{\frac{-E_a}{RT}}\right)^{\frac{1}{z}}}{3600 \times 20^{\frac{1}{z}}} \tag{33}$$
$$C_{rate} = \frac{|i(t)|}{C_c} \tag{34}$$
$$E_a = 31700 - 370.3 \times C_{rate} \tag{35}$$

where C_{rate} is the ratio of the battery current to the capacity of a new battery C_c shown in (34), E_a is the Li-ion battery activation energy shown in (35), T is the absolute temperature in Kelvin, R is the gas constant 0.8314 $Jmol^{-1}K^{-1}$, z is the power law factor of 0.55 and B is a parameter obtained from empirically curve fitting the data in Table 5 [5], [6], [51], [54]. A battery C_{rate} of 1C is the battery current required to discharge the battery in one hour [53]. Therefore, for a 4 Ah battery, a C_{rate} of 1C represents 4 A of current. In this work, the range of current for the 4 Ah battery bank was between [0, 1.2] A corresponding to a C_{rate} range of [0, 0.3] C. Furthermore, the parameter B varied between [36041.7, 33324.08] upon curve fitting based on the information in Table 5. Equation (33) captures the impact of the instantaneous battery current on the battery capacity degradation and is used in this work to obtain the SOH degradation at every time instant.

4) ESTIMATION OF BATTERY BANK RUNTIME AND LIFETIME

The complete battery bank runtime and lifetime were obtained offline using the CM battery model. The battery

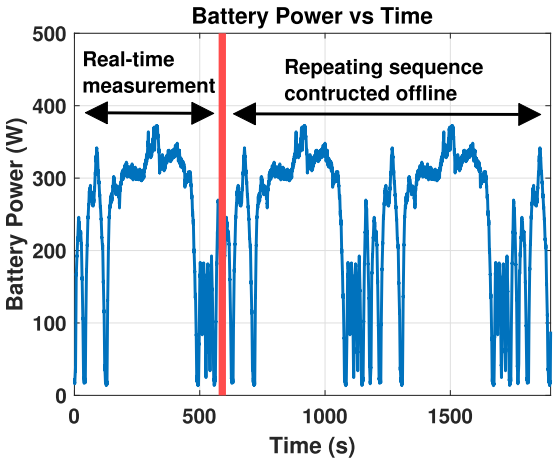

FIGURE 7. Battery power constructed in a repeating sequence.

power consumption recorded from the real-time implementation over the duration of the drive cycles is arranged in a repeating sequence as shown in Fig. 7. The battery bank current in Fig. 8a is obtained by dividing the repeating sequence of battery bank power by the battery bank voltage obtained from the CM model. The increase in battery current over time due to a drop in battery bank voltage, shown in Fig. 8b, is captured and used with (31) to accurately compute the battery bank SOC. The time required for the SOC to drop from 100% to 20% represents the battery bank runtime. Furthermore, the SOH was obtained by taking the average of the battery bank current and substituting it in (33). The time required for the SOH to drop from 100% to 80% represents the battery bank lifetime and signals the EOL of the battery bank [5], [6]. The overall process of estimating the battery bank runtime and lifetime is summarized in Fig. 9.

E. HARDWARE SETUP SPECIFICATION

Fig. 10 shows the complete EV traction system that has been developed in the Renewable Energy Research Center at the American University of Sharjah. The detailed specifications of the experimental setup are provided in Table 6. Starting from the right, a 400 V, 4.0 Ah Li-ion battery bank powers a three-phase IGBT inverter. The inverter converts the battery bank DC voltage into the necessary AC voltage and frequency required to drive the IM at the required speed. A dynamometer is used to apply the mechanical load on the motor. The dynamometer applied a constant 2 Nm load throughout the duration of the NEDC and US06 drive cycles. The motor speed and motor torque under the dynamometer load are recorded and are displayed in Fig. 11. Figs. 11a and 11b show that the motor is supplying the required 2 Nm load while tracking the speed for the NEDC and US06 drive cycles respectively. The control algorithm is created on MATLAB/Simulink 2013b and is shown in Fig. 12. The maroon blocks are the gains used for ADC conversion. The red blocks represent the references in the system such as the drive cycle and the reference motor d-axis current i^*_{sd}. The slip

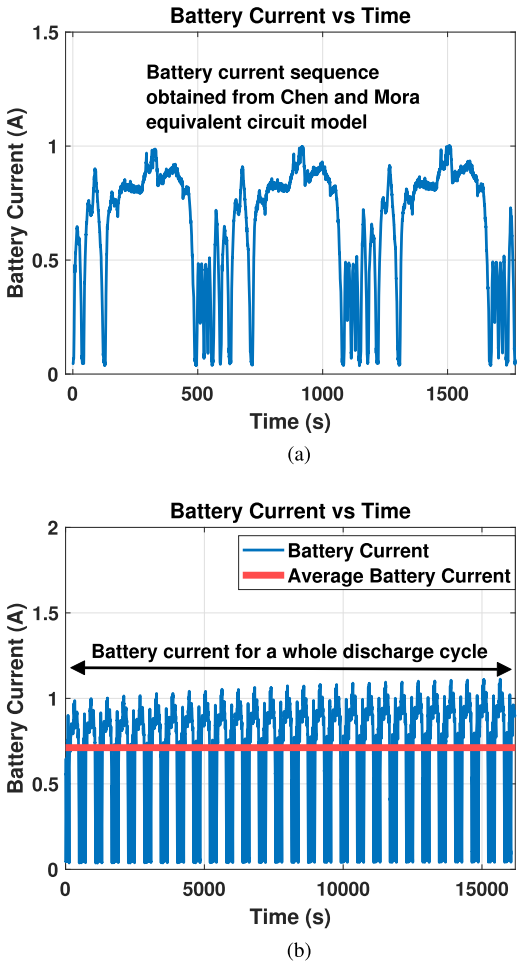

FIGURE 8. (a) Battery current sequence obtained from the Chen and Mora equivalent circuit model, (b) Battery current in one cycle.

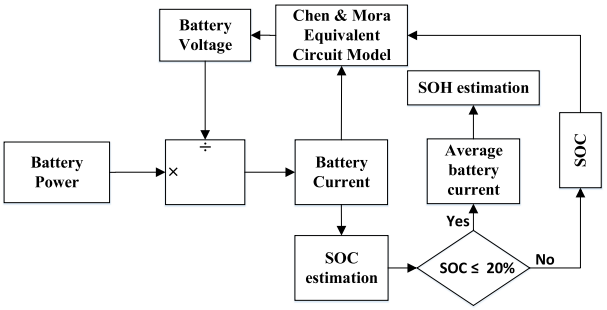

FIGURE 9. Flowchart for obtaining the battery bank runtime and lifetime.

frequency estimation block estimates the rotor flux and slip using (8) and (9) respectively. The orange blocks represent the dSPACE 1103 controller blocks. They are the ADC channels 17,18,19, 5 which measure the motor phase currents, the battery bank current and voltage, the encoder block used to measure the motor speed, and the PWM3 block used to generate the inverter gating signals from the duty cycles respectively. The battery calculations block performs the SOC and SOH estimation using (31) and (33) then sends the SOC to the proposed controllers. The cyan blocks represent the controllers in the system. The 'Proposed Controllers' block

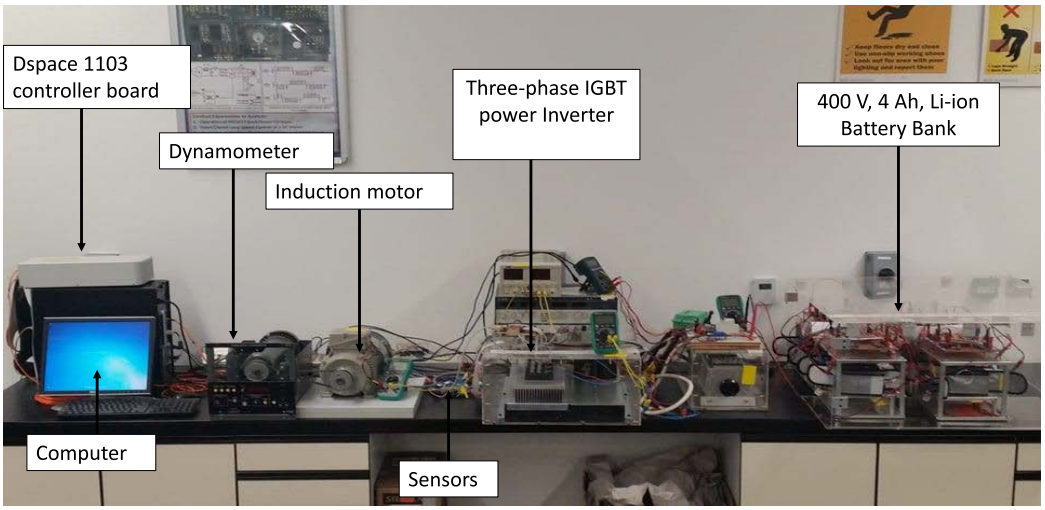

FIGURE 10. Li-ion battery bank powered EV traction system experimental setup.

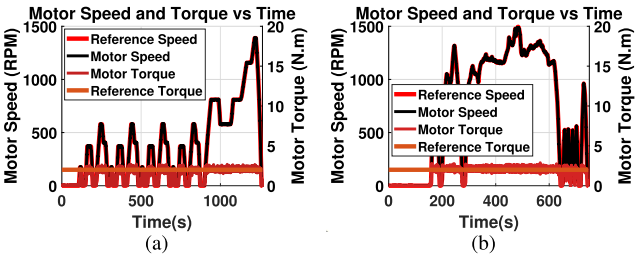

FIGURE 11. (a) Motor speed and torque curves for the NEDC drive cycle, (b) Motor speed and torque curves for the US06 drive cycle.

TABLE 6. EV traction system experimental setup specifications.

Component	Parameter	Value
Induction motor	Nominal voltage	400 V-Y, 50 Hz
	Nominal current	4.65 A
	Nominal power	2.2 kW
	Nominal power factor	0.81
	Nominal speed	1455 RPM
	Motor efficiency	85%
	Poles pairs	2
	Stator resistance (R_s)	3.24 Ω
	Rotor resistance (R_r)	1.31 Ω
	Stator leakage inductance (L_{ls})	0.0458 H
	Rotor leakage inductance (L_{lr})	0.0102 H
Drive system specifications	Inverter rating	500 V, 10 A
	Controller board	dSPACE 1103
	Sampling time	100 μs
	Encoder resolution	1024 pulses per revolution
	Voltage sensor	(LEM LV-25 P) 500 V
	Current sensor	(LEM LA-25 NP) 25 A
Li-ion battery bank specifications	Battery model (Lithium-Polymer)	ACE30-4000-0601
	Number of batteries	16
	Battery bank capacity	4.0 Ah
	Nominal voltage of each battery	22.2 V
	Maximum voltage of each battery	25.2 V
	Maximum battery bank voltage	403.2 V

contains the proposed CSFLC and FMPC BEM controllers, while the two inner PI controllers regulate the motor i_{sd} and i_{sq} currents. The reference voltage commands V_{sd}^* and V_{sq}^* produced by the two inner PI controllers are converted through the dq/abc transformation to V_a^*, V_b^*, and V_c^* reference sinusoidal voltages that are used by the PWM generation block to generate the inverter duty cycles D_a, D_b, D_c. The MATLAB/Simulink model is converted to C-language, then uploaded into the dSPACE 1103 controller board. The dSPACE 1103 controller board is interfaced with the computer, this allows for real-time monitoring and control of the EV traction system. The communication between the user and the dSPACE 1103 controller board is done through the ControlDesk 5.2 software. ControlDesk 5.2 performs various real-time tasks such as displaying the measured current and SOC of the Li-ion battery bank and controlling the IM drive.

III. PROPOSED BEM STRATEGIES FOR EV TRACTION SYSTEM

A. FUZZY LOGIC CONTROLLER (FLC)

The FLC architecture used for speed regulation is shown in Fig. 13. The FLC produces the change in the torque regulating current signal at instant k denoted by $\Delta i_{sq}^*(k)$. It monitors the motor speed error $e(k)$, and the change in error $\Delta e(k)$, between the reference speed $\omega_r^*(k)$, and the motor speed $\omega_{mech}(k)$. Fig. 13 shows the 3 stages that the signal passes through before a command is issued by the controller. The first stage is the fuzzification stage and it converts the signal into linguistic variables [19], [37]. The second stage is the fuzzy inference engine which takes the linguistic variables and compares them with the rule base then generates a linguistic output [19], [37]. The final stage is the defuzzification stage and it converts the linguistic outputs to the command signal [55], [56]. The FLC produces the change in the control signal $\Delta i_{sq}^*(k)$, and adds it to the current value $i_{sq}(k-1)$ to form $i_{sq}^*(k)$.

The FLC is used in the speed regulator block in Fig. 1. The surface summarizing the fuzzification, inference mechanism for the normalized motor speed error $e(k)$ and the normalized change in speed error $\Delta e(k)$, and the defuzzification into

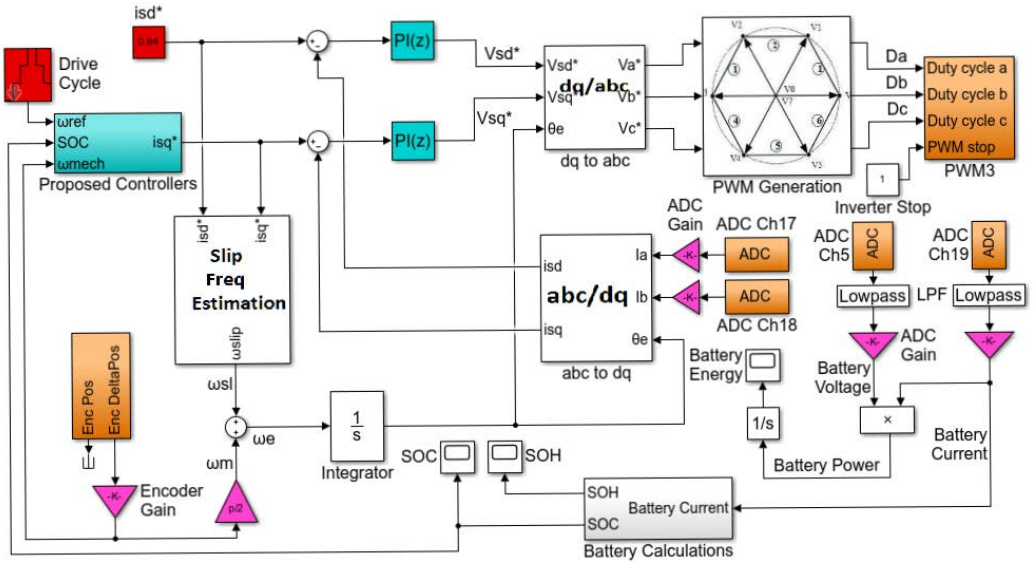

FIGURE 12. MATLAB/Simulink model for EV traction system experimental testing.

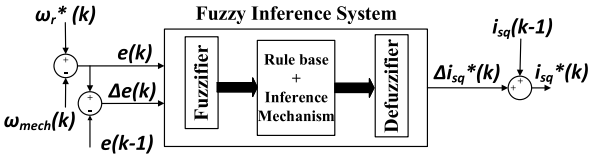

FIGURE 13. FLC speed regulator block diagram.

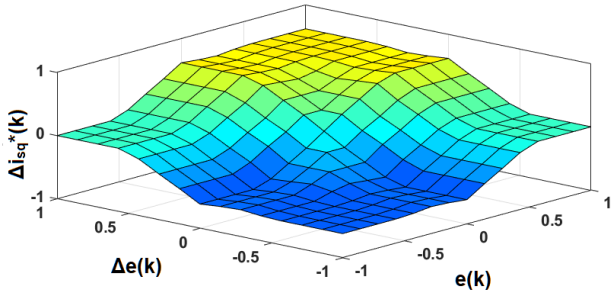

FIGURE 14. FLC speed regulator surface.

Δi^*_{sq} is shown in Fig. 14. The surface illustrates that when $e(k)$ and $\Delta e(k)$ are between [0.5, 1], then Δi^*_{sq} is positive and a large increase in the torque regulating current Δi^*_{sq} is required. When $e(k)$ and $\Delta e(k)$ are between [-1, -0.5] then a large decrease in Δi^*_{sq} is required. When $e(k)$ and $\Delta e(k)$ are between [-0.5, 0.5], then the magnitude of Δi^*_{sq} is dependent upon their intersection with the surface. A small increase or decrease in Δi^*_{sq} is provided until $e(k)$ and $\Delta e(k)$ approach 0. The range of operation for $e(k)$ and $\Delta e(k)$ before normalizing was [-1500, 1500] RPM while the range of operation of Δi^*_{sq} before normalizing was between $[-3, 3]$ A.

The FLC speed regulator is implemented and the values of the energy, SOC, and SOH are recorded and compared with the CSFLC BEM technique. The proposed CSFLC technique is presented in the next section, and it performs the energy management operation with minimal degradation in the speed tracking performance.

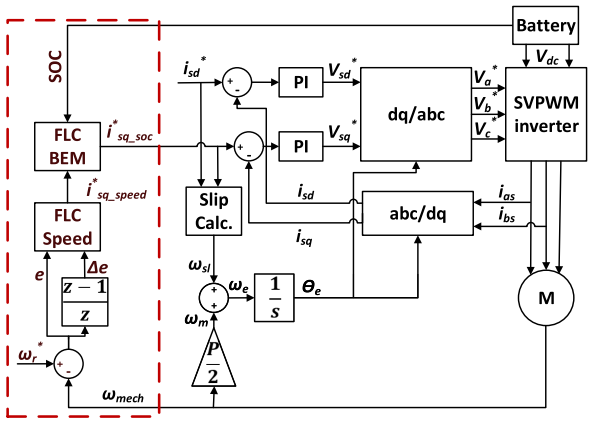

FIGURE 15. Proposed CSFLC BEM IM drive system.

B. PROPOSED BEM TECHNIQUE 1: CASCADED FLC (CSFLC)

The CSFLC technique is designed using two cascaded FLCs as shown in the red box in Fig. 15. The first FLC labeled "FLC Speed" in Fig. 15, generates the desired current $i^*_{sq\_\,speed}$ to regulate the motor speed. While the second FLC labeled "FLC BEM" acts as a variable gain which limits the variations in $i^*_{sq\_\,speed}$ based on the battery's SOC, and produces $i^*_{sq\_\,soc}$. The slip calculation block estimates the rotor flux then calculates the slip using (8) and (9) respectively. Furthermore, the d-axis current i^*_{sd} regulates the motor flux while the q-axis current $i^*_{sq\_\,soc}$ regulates the motor torque. In contrast to the q-axis current i^*_{sq} generated by a regular speed controller, the q-axis current $i^*_{sq\_\,soc}$ generated by the CSFLC BEM technique contains fewer current variations. As a result, less battery bank current is consumed and the battery energy is conserved. The two inner PI controller loops compare the motor i_{sd} and i_{sq} currents with the reference i^*_{sd}

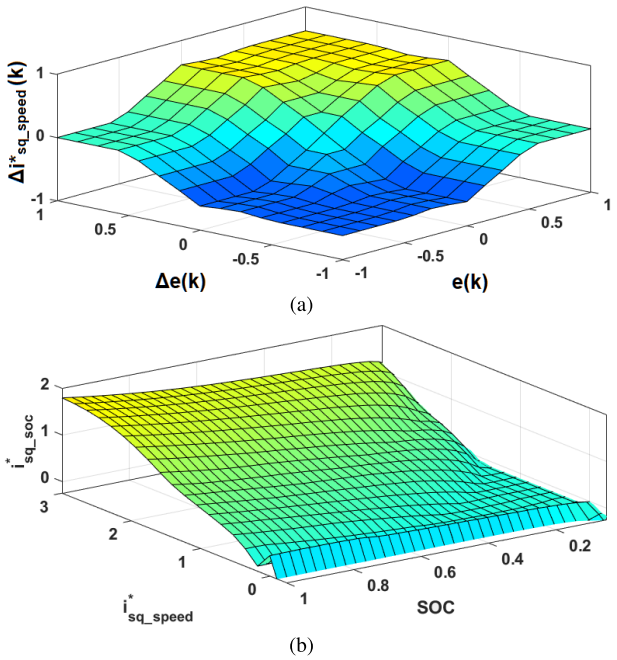

FIGURE 16. (a) Surface describing the "FLC Speed" block in the CSFLC IM drive, (b) Surface describing the "FLC BEM" block in the CSFLC IM drive.

and $i^*_{sq\_soc}$ currents and ensure that they are equal during the operation of the EV traction system. The errors produced by the two inner PI controllers are used to generate the reference voltage commands V^*_{sd} and V^*_{sq} respectively. These reference voltages are converted through the dq/abc transformation to V^*_a,V^*_b, V^*_c reference sinusoidal voltages that are used to generate PWM signals for the inverter. The surface describing the relationship between the inputs and output of both FLCs is shown in Fig. 16. The first surface shown in Fig. 16a, shows the relationship between the motor speed error $e(k)$ and change in motor speed error $\Delta e(k)$, the output is the desired change in the torque regulating current signal $\Delta i^*_{sq\_speed}(k)$. The $\Delta i^*_{sq\_speed}(k)$ signal is added to the current signal $i_{sq\_speed}(k-1)$ to form $i^*_{sq\_speed}$ which regulates the motor speed without taking battery SOC into account. This surface used is the same as the surface for the conventional FLC speed regulator described in the previous section. While the second surface, shown in Fig. 16b, displays the modification to $i^*_{sq\_speed}$ that incorporates the battery's SOC such that the energy saving signal $i^*_{sq\_soc}$ is produced instead. The surface scales the $i^*_{sq\_speed}$ signal into a smoother $i^*_{sq\_soc}$ with less ripples at all values. A spike in the surface serves to suppress the high $i^*_{sq\_speed}$ ripples that were observed during experimentation at zero $i^*_{sq\_speed}$, such that they do not appear in $i^*_{sq\_soc}$. An $i^*_{sq\_speed}$ signal rippling between [2, 3] A has a ripple range of 1 A, while an $i^*_{sq\_soc}$ signal will ripple between [1.3, 1.8] A which has a ripple range of 0.5 A. This means that less current is demanded, thus more battery SOC is conserved. Fig. 17 shows a flowchart integrating the CSFLC technique with the EV traction system. The motor speed is measured, compared

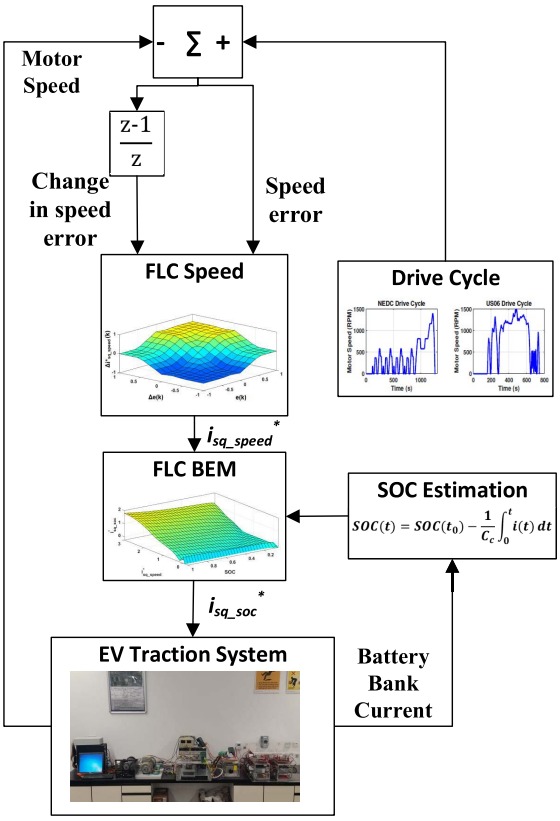

FIGURE 17. Flowchart for the proposed CSFLC BEM technique.

with the drive cycle then the motor speed error and the change in motor speed error are sent to the "FLC Speed" block. The "FLC Speed" block generates the $i^*_{sq\_speed}$ required to regulate the motor speed. On the other hand, the battery bank current is measured, and an estimation of the SOC is sent to the "FLC BEM" block which acts as a variable gain by scaling the $i^*_{sq\_speed}$ signal into the new $i^*_{sq\_soc}$ signal, thus taking the battery information into account when producing $i^*_{sq\_soc}$. The $i^*_{sq\_soc}$ signal regulates the motor speed while conserving battery energy.

C. MODEL PREDICTIVE CONTROLLER (MPC)

An MPC uses the dynamic model of the system to compute the optimal control signal required to make the system output achieve a reference value. The MPC contains two parameters that need to be chosen depending on the system. The first parameter is the prediction horizon N_p and it represents the number of output future samples the controller can predict. Whereas, the control horizon N_c is the number of output future samples the controller can control ($N_p \geq N_c$).

Consider a system with an output that does not directly depend on the control signal at sampling instant k. The system is represented by the discrete time state-space model in (36) and (37).

$$x_m(k+1) = A_m x_m(k) + B_m u(k) \tag{36}$$

$$y(k) = C_m x_m(k) \tag{37}$$

The difference between the current and previous value of the control signal Δu, and the state variable Δx_m, is defined in (38) and (39).

$$\Delta u(k) = u(k) - u(k-1) \tag{38}$$
$$\Delta x_m(k) = x_m(k) - x_m(k-1) \tag{39}$$

Combining (36) - (39) we form (40) and (41).

$$\Delta x_m(k+1) = A_m \Delta x_m(k) + B_m \Delta u(k) \tag{40}$$
$$\begin{aligned} y(k+1) &= y(k) + C_m \Delta x_m(k+1) \\ &= y(k) + C_m A_m \Delta x_m(k) + C_m B_m \Delta u(k) \end{aligned} \tag{41}$$

Equations (40) and (41) can be used to form the augmented state-space model of the system represented by (42) and (43).

$$x(k+1) = Ax(k) + B\Delta u(k) \tag{42}$$
$$y(k) = Cx(k) \tag{43}$$

where

$$x(k) = \begin{bmatrix} \Delta x_m(k) \\ y(k) \end{bmatrix},\ A = \begin{bmatrix} A_m & 0_m^T \\ C_m A_m & 1 \end{bmatrix},$$
$$B = \begin{bmatrix} B_m \\ C_m B_m \end{bmatrix},\ C = \begin{bmatrix} 0_m & 1 \end{bmatrix}.$$

and $0_m = [0, 0, \cdots 0]$ is used to fill up the empty spaces in the matrices.

Using the augmented model, the plant output is predicted over the prediction horizon N_p. Given that we are currently in sampling instant k, the general form of the new system states, as expressed in (44), is obtained by expanding $x(k+1)$ in the augmented state-space model in (42) for every future sample.

$$\begin{aligned} x(k+1|k) &= Ax(k) + B\Delta u(k) \\ &\vdots \\ x(k+N_p|k) &= A^{N_p}x(k) + A^{N_p-1}B\Delta u(k) + \cdots \\ &\quad + A^{N_p-N_c}B\Delta u(k+N_c-1) \end{aligned} \tag{44}$$

Similarly, the general form, in (45), of the predicted output y is obtained by expanding $y(k)$ for future samples in the augmented state-space model in (43).

$$\begin{aligned} y(k+1|k) &= CAx(k) + CB\Delta u(k) \\ &\vdots \\ y(k+N_p|k) &= CA^{N_p}x(k) + CA^{N_p-1}B\Delta u(k) + \cdots \\ &\quad + CA^{N_p-N_c}B\Delta u(k+N_c-1) \end{aligned} \tag{45}$$

The vector ΔU represents the current and future change in the control signal, with dimension N_c, and the vector Y represents the predicted future output, with dimension N_p, are defined by (46) and (47) respectively.

$$\Delta U = [\Delta u(k)\ \Delta u(k+1)\ \cdots \Delta u(k+N_c-1)]^T \tag{46}$$
$$Y = [y(k+1|k)\ y(k+2|k)\ \ldots\ y(k+N_p|k)]^T \tag{47}$$

Combining (44) - (47) yields (48).

$$Y = Fx(k) + \Phi\Delta U(k) \tag{48}$$

where

$$F = \begin{bmatrix} CA \\ CA^2 \\ \vdots \\ CA^{N_p} \end{bmatrix}$$

and

$$\Phi = \begin{bmatrix} CB & 0 & \cdots & 0 \\ CAB & CB & \cdots & 0 \\ CA^2B & CAB & \cdots & 0 \\ \vdots & \vdots & \ddots & \vdots \\ CA^{N_p-1}B & CA^{N_p-2}B & \cdots & CA^{N_p-N_c}B \end{bmatrix}.$$

The vector containing the reference signal of the system has a length of N_p and is defined by (49).

$$R_s^T = [1\ 1 \cdots 1]r(k) \tag{49}$$

A cost function J, is defined to reflect the control objective and is represented by (50).

$$J = (R_s - Y)^T \bar{Q}(R_s - Y) + \Delta U^T \bar{R} \Delta U \tag{50}$$

where $\bar{R} = R_{N_c \times N_c}$ and $\bar{Q} = Q_{N_p \times N_p}$ are the input and output weight matrices. The weights can be modified depending on the operation. The ratio of the input weight R to the output weight Q, penalizes the control signal variations during the system's operation. Therefore in this work, the output weight Q is set to unity, and the input weight R is manipulated during operation. The cost function in (50) can be expanded by substituting Y from (48) into (50). After such expansion, the partial derivative with respect to ΔU is taken and equated to zero yielding equations (51) - (52).

$$\frac{\partial J}{\partial \Delta U} = -2\Phi^T(R_s - Fx(k)) + 2(\Phi^T\Phi + \bar{R})\Delta U \tag{51}$$
$$\frac{\partial J}{\partial \Delta U} = 0 \rightarrow \Delta U = (\Phi^T\Phi + \bar{R})^{-1}\Phi^T(R_s - Fx(k)) \tag{52}$$

The first element of ΔU is added to the previous control signal $u(k-1)$ to obtain the current control signal $u(k)$.

The MPC is used in the speed regulator block shown in Fig. 1. The battery bank energy, SOC, and SOH results were recorded and compared with the FMPC BEM technique. The proposed FMPC technique is presented in the next section, and it performs the energy management operation with minimal degradation in the motor speed tracking performance.

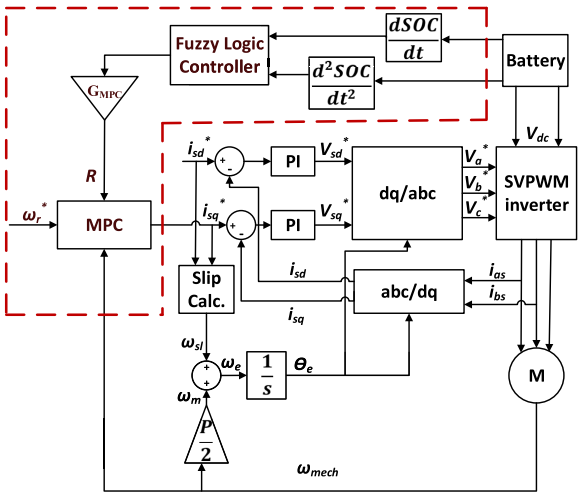

FIGURE 18. Proposed FMPC IM drive system.

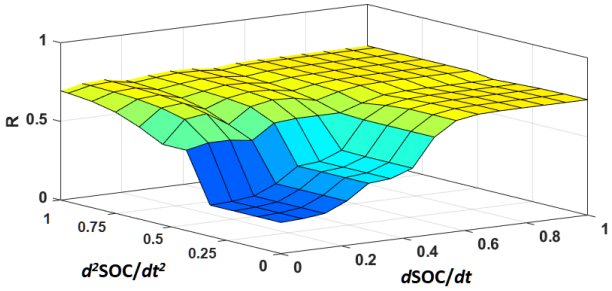

FIGURE 19. Weight tuning FLC surface in the FMPC IM drive.

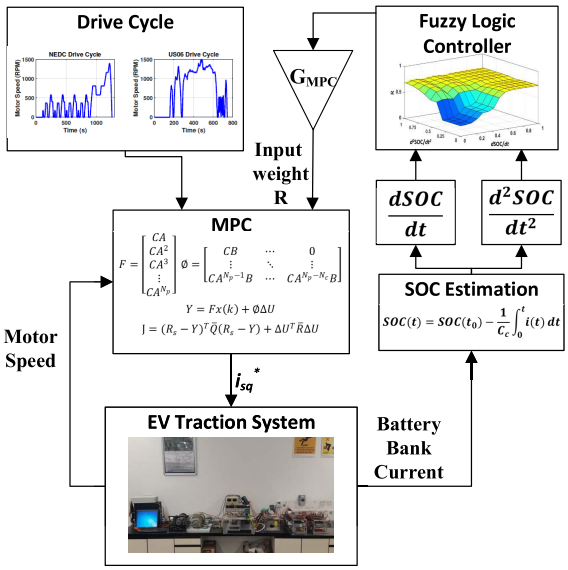

FIGURE 20. Flowchart for the proposed FMPC BEM technique.

D. PROPOSED BEM TECHNIQUE 2: FUZZY MPC (FMPC)

The second BEM technique, shown in Fig. 18 in the red box, employs an MPC which generates a reference current i^*_{sq} to regulate the motor speed. An FLC adjusts the input weight of the MPC to penalize the i^*_{sq} variations by taking into account the battery's $dSOC/dt$ and d^2SOC/dt^2. The battery's $dSOC/dt$ was evaluated by taking the difference between the current SOC value and the previous SOC value and the d^2SOC/dt^2 was evaluated by taking the difference between the current and previous $dSOC/dt$. The $dSOC/dt$ and the d^2SOC/dt^2 are normalized between [0, 1]. The slip calculation obtains the rotor flux and slip using (8) and (9) respectively. In addition, the d-axis current i^*_{sd} regulates the motor flux while the q-axis current i^*_{sq} regulates the motor torque. Like the CSFLC technique, the FMPC BEM technique generates a reference q-axis current i^*_{sq} with less current fluctuations as compared to the q-axis current i^*_{sq} generated by the conventional MPC speed controller. The current fluctuations vary depending on the value of the input weight R. In other words, the input weight needs to be regulated in real-time to reduce the i^*_{sq} fluctuations. This will lead to a lower battery current consumption, and preserve battery energy. With regards to the two inner PI controller loops, they regulate the motor i_{sd} and i_{sq} currents such that they are equal to the reference i^*_{sd} and i^*_{sq} currents. Furthermore, the two inner PI controllers generate the reference voltage commands V^*_{sd} and V^*_{sq} which are converted through the dq/abc transformation to V^*_a, V^*_b, and V^*_c reference sinusoidal voltages. These sinusoidal voltages are used to generate PWM signals for the inverter. The surface describing the relationship between the input weight and the battery's $dSOC/dt$ and d^2SOC/dt^2 is shown in Fig. 19. The surface can be divided into 3 regions, the first region occurs when the $dSOC/dt$ is between [0.5, 1] for all d^2SOC/dt^2 values and the second region occurs when d^2SOC/dt^2 is between [0.5, 1] for all values of $dSOC/dt$. These regions indicate that there is an abrupt increase in battery current and that the SOC is declining rapidly which occurs due to motor acceleration. Therefore, a limitation must be placed on i^*_{sq}, thus a large input weight R is produced from the controller. The third region is the input weight transition region and it is responsible for producing different input weights at different steady state values of the system. The third region occurs when $dSOC/dt$ is between [0, 0.5] and d^2SOC/dt^2 is between [0, 0.5] and its objective is to tune the input weight R for different motor speeds such that the battery SOC consumption is minimized. The gain G_{MPC} is set by the user and it controls the maximum value of the input weight R. The maximum G_{MPC} value that made a visible difference in i^*_{sq} variations is 20. Therefore, G_{MPC} is set to 20 in this work. Fig. 20 shows a flowchart integrating the FMPC technique with the EV traction system. The motor speed and the drive cycle information are sent to the MPC block. Furthermore, the battery bank current is measured and the SOC is estimated. The first and second derivatives of the SOC are sent to the fuzzy logic controller block which with the gain G_{MPC}, generates an input weight R for the MPC block such that the battery information is taken into account

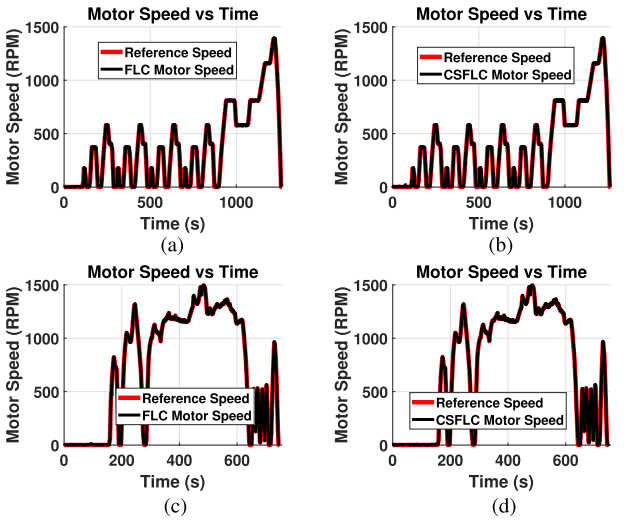

FIGURE 21. (a) FLC speed response under the NEDC drive cycle, (b) CSFLC speed response under the NEDC drive cycle, (c) FLC speed response under the US06 drive cycle, (d) CSFLC speed response under the US06 drive cycle.

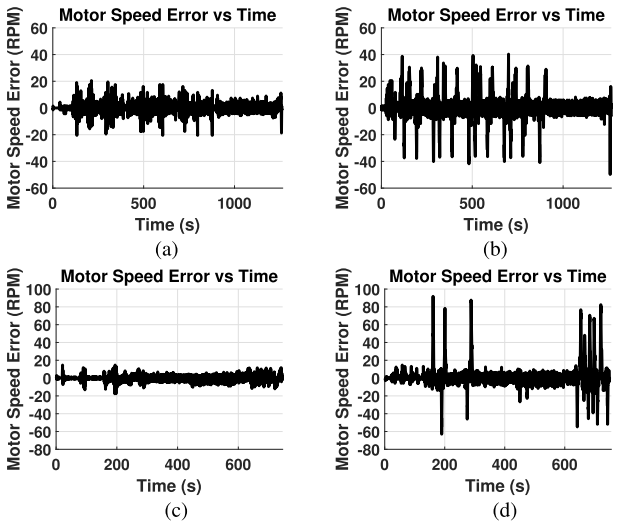

FIGURE 22. (a) FLC speed error under the NEDC drive cycle, (b) CSFLC speed error under the NEDC drive cycle, (c) FLC speed error under the US06 drive cycle, (d) CSFLC speed error under the US06 drive cycle.

when generating i^*_{sq}. The MPC generates an i^*_{sq} that regulates the motor speed while preserving battery energy.

IV. EXPERIMENTAL VALIDATION OF ENERGY MANAGEMENT TECHNIQUES ON EV TRACTION SYSTEM

A hardware implementation of the two BEM techniques along with the conventional FLC and MPC speed regulators is presented in this section. The motor's speed performance, current i^*_{sq} and battery bank current, energy, SOC, and SOH are recorded for both the NEDC and US06 drive cycles then the runtime and lifetime were estimated. The experimental results are discussed then a summary of the information is tabulated in this section.

A. CSFLC BEM TECHNIQUE

1) SPEED REGULATION

Fig. 21 shows the speed response for the FLC and CSFLC with the NEDC and US06 drive cycles. Figs. 21a - 21d show that both controllers are tracking the drive cycle reference speed as intended. Fig. 22 shows the error in speed tracking for the FLC and CSFLC techniques. Figs. 22a - 22d show that the speed errors converge to zero. The absolute average error was 1.28 and 1.69 for the FLC, whereas it was 3.7 and 6.93 for the CSFLC with the NEDC and US06 drive cycles respectively. These values indicate that the CSFLC experiences a degradation in speed tracking performance as compared to the FLC speed regulator.

2) CURRENT CONSUMPTION

The motor's torque regulating current command i^*_{sq}, is displayed in Fig. 23. Figs. 23a and 23b show the extent of the control effort applied by the FLC to regulate the speed of the EV traction system during the drive cycles. While Figs. 23c and 23d show the effect of taking the SOC into account while

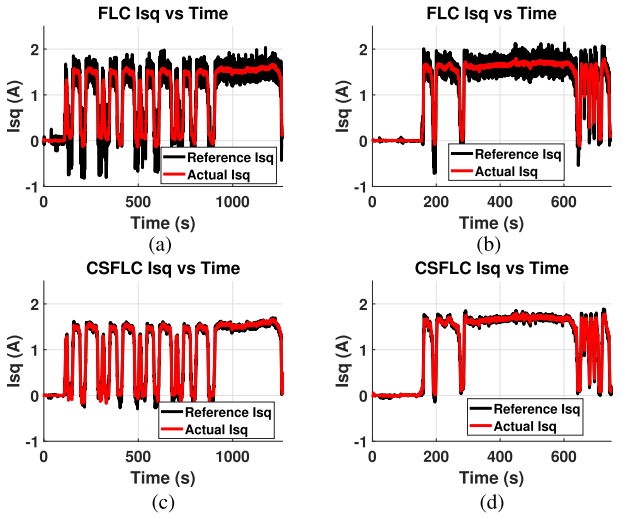

FIGURE 23. (a) FLC current i^*_{sq} with the NEDC drive cycle, (b) FLC current i^*_{sq} with the US06 drive cycle, (c) CSFLC current i^*_{sq} with the NEDC drive cycle, (d) CSFLC current i^*_{sq} with the US06 drive cycle.

deciding i^*_{sq}. It is evident that the i^*_{sq} variation has substantially reduced when a second FLC is cascaded with the first FLC. Figs. 23a and 23b clearly show that a large control effort is exerted by the first FLC as it regulates the speed. While Figs. 23c and 23d display a smaller control effort as it diminishes the current variation while regulating the motor speed. To quantify this observation, the average of the absolute value of i^*_{sq} is taken and is denoted by $i^*_{sq\ avg}$. For the NEDC and US06 drive cycles respectively, the FLC had an $i^*_{sq\ avg}$ of 1.0741 A and 1.1842 A, while the $i^*_{sq\ avg}$ for the CSFLC is 1.0543 A and 1.1524 A. We can conclude that the CSFLC BEM strategy demands less i^*_{sq} than the conventional FLC to regulate the motor speed. Fig. 24 shows the battery bank current production with the NEDC and US06 drive cycles.

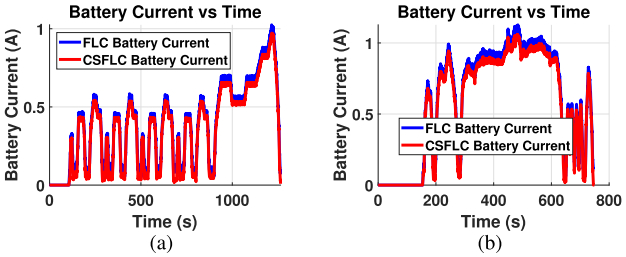

FIGURE 24. (a) Li-ion battery bank current profile of FLC and CSFLC with the NEDC drive cycle, (b) Li-ion battery bank current profile of FLC and CSFLC with the US06 drive cycle.

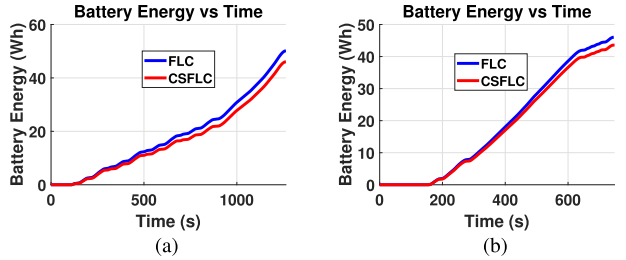

FIGURE 25. (a) FLC and CSFLC battery energy consumption with the NEDC drive cycle, (b) FLC and CSFLC battery energy consumption with the US06 drive cycle.

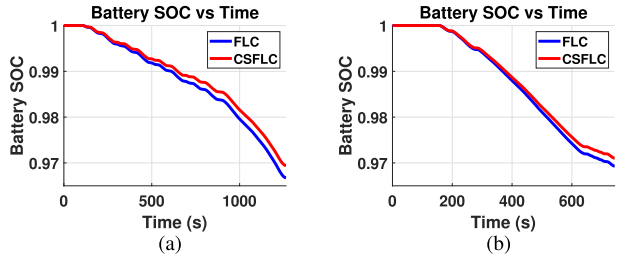

FIGURE 26. (a) SOC variation of the Li-ion battery bank with the NEDC drive cycle for FLC and CSFLC, (b) SOC variation of the Li-ion battery bank with the US06 drive cycle for FLC and CSFLC.

Figs. 24a and 24b show that the FLC consistently consumes a higher current than the CSFLC in both drive cycles. The FLC battery bank current ranges from [0, 1.04] A and [0, 1.14] A, while it ranges between [0, 0.98] A and [0, 1.08] A for CSFLC with the NEDC and US06 drive cycles respectively. Furthermore, the average battery bank current $i_{bat\ avg}$, occurs at 0.3786 A and 0.5939 A for FLC, while it occurs at 0.3473 A and 0.5574 A for CSFLC with the NEDC and the US06 drive cycles respectively. Thus, the proposed CSFLC consumes an overall lower average current with both drive cycles as compared to the conventional FLC controller controlling the speed of EV traction system alone.

3) BATTERY BANK ENERGY, SOC, SOH, RUNTIME AND LIFETIME MEASUREMENTS

Fig. 25 shows the energy consumed from the battery bank by the EV traction system. The FLC consumed 50.13 Wh and 46.03 Wh, whereas the CSFLC consumed 46.01 Wh and 43.56 Wh yielding an improvement of 8.2% and 5.4% with the NEDC and US06 drive cycles respectively. Figs. 26 and 27 show the trend in SOC and SOH with the NEDC and US06 drive cycles.

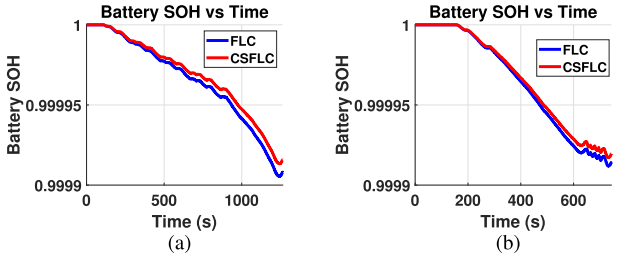

FIGURE 27. (a) SOH variation of the Li-ion battery bank with the NEDC drive cycle for FLC and CSFLC, (b) SOH variation of the Li-ion battery bank with the US06 drive cycle for FLC and CSFLC.

The FLC shows a larger degradation than the CSFLC for both the SOC and SOH on both drive cycles. The final value of the SOC for the FLC is 0.9668 and 0.9694 yielding an SOC consumption of 0.0332 and 0.0306, while the final SOC values for the CSFLC changed to 0.9695 and 0.9712 yielding an SOC consumption of 0.0305 and 0.0288 with the NEDC and US06 drive cycles respectively. The CSFLC has reduced the SOC consumption by 8.1% and 5.9% with the NEDC and US06 drive cycles. Furthermore, the final value of the SOH for the FLC is 0.999908 and 0.9999145 yielding an SOH degradation of 0.000092 and 0.0000855, while the CSFLC final SOH values were 0.99991568 and 0.99992 yielding an SOH degradation of 0.00008432 and 0.00008 with the NEDC and US06 drive cycles respectively. The CSFLC reduced the SOH degradation by 8.3% and 6.4% with the NEDC and US06 drive cycles. In addition, the FLC runtime is 7.208 hours and 3.981 hours, while the CSFLC runtime is 7.857 hours and 4.193 hours with the NEDC and US06 drive cycles respectively. Therefore, there was an increase in runtime by 0.649 hours (38 minutes 56 seconds) and 0.212 hours (12 minutes 43 seconds); in other words, 9% and 5.3% improvement in overall runtime. While the lifetime for the FLC expires after 70075.5 hours and 34952.8 hours, whereas for the CSFLC it ends after 73992.5 hours and 37098.5 hours with the NEDC and US06 drive cycles respectively. The CSFLC resulted in an increase of 3917 hours and 2145.7 hours corresponding to a 5.6% and 6.1% increase in battery lifetime over the course of the NEDC and US06 drive cycles respectively.

It is clear from the graphical presentation that the motor current has many fluctuations in Fig. 23a and 23b as compared to 23c and 23d. The CSFLC technique managed to eliminate such fluctuations which led to a lower consumption in battery current. Consequently, less battery energy was consumed. The decrease in battery current can be noticed in Fig. 24. In Figs. 24a and 24b, the battery current consumed by the CSFLC was lower than the battery current consumed by the FLC with the NEDC and US06 drive cycles. Due to a reduction in battery current consumption, the battery energy, SOC, and SOH consumption were also reduced as shown in Figs. 25, 26, and 27 respectively. In Figs. 25a and 25b, 26a and 26b, and 27a and 27b the battery energy, SOC, and SOH degradation were lower with the CSFLC than

TABLE 7. Summary of the experimental results for FLC and CSFLC.

Measurements \ Controllers	NEDC			US06		
	FLC	CSFLC	Savings	FLC	CSFLC	Savings
Absolute Average Error (RPM)	**1.28**	3.7	-	**1.69**	6.93	-
Control Effort $i^*_{sq\ avg}$ (A)	1.0741	**1.0543**	-	1.1842	**1.1524**	-
Battery Current $i_{bat\ avg}$ (A)	0.3786	**0.3473**	-	0.5939	**0.5574**	-
Final SOC (%)	96.68	**96.95**	8.1%	96.94	**97.12**	5.9%
Final SOH	0.999908	**0.99991568**	8.3%	0.9999145	**0.99992**	6.4%
Battery Energy (Wh)	50.13	**46.01**	8.2%	46.03	**43.56**	5.4%
Estimated Runtime (hours)	7.208	**7.857**	9%	3.981	**4.193**	5.3%
Estimated Lifetime (hours)	70075	**73992**	5.6%	34952	**37098**	6.1%

The bold values indicate the best value (maximum or minimum).

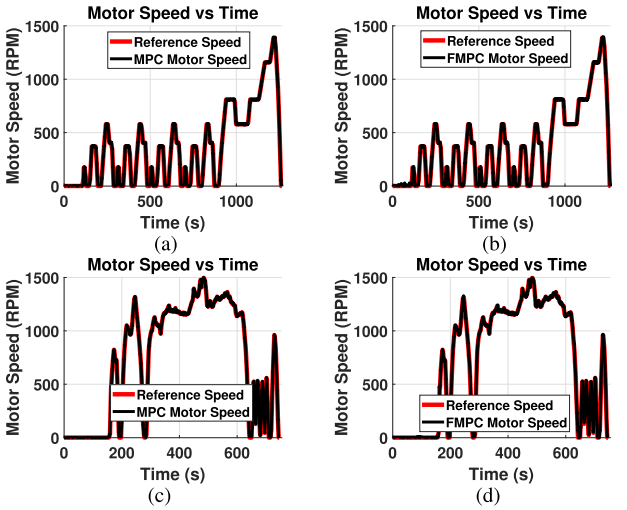

FIGURE 28. (a) MPC speed response under the NEDC drive cycle, (b) FMPC speed response under the NEDC drive cycle, (c) MPC speed response under the US06 drive cycle, (d) FMPC speed response under the US06 drive cycle.

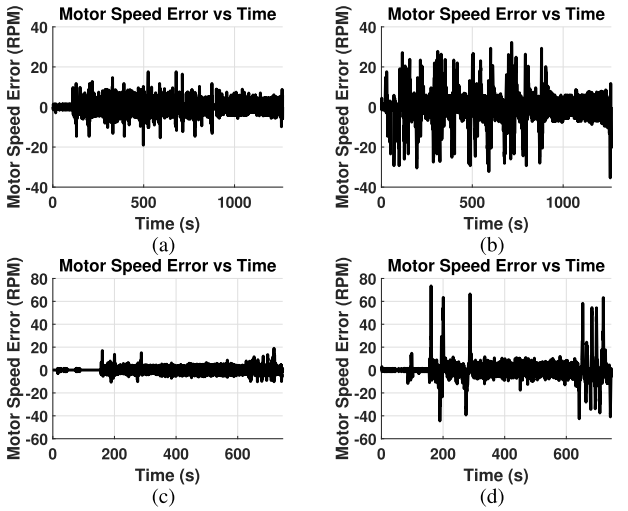

FIGURE 29. (a) MPC speed error under the NEDC drive cycle, (b) FMPC speed error under the NEDC drive cycle, (c) MPC speed error under the US06 drive cycle, (d) FMPC speed error under the US06 drive cycle.

with the FLC for the NEDC and US06 drive cycles respectively. Overall, the CSFLC technique consumed less energy, SOC, and SOH from the battery bank while extending its runtime and lifetime. We conclude that the CSFLC not only enhances the IM drive energy management, but also elongates the battery life. A summary of the results is presented in Table 7.

B. FMPC BEM TECHNIQUE

1) SPEED REGULATION

Fig. 28 shows the speed response for the MPC and FMPC with the NEDC and US06 drive cycles. Figs. 28a - 28d show that both controllers are regulating the speed for the NEDC and US06 drive cycles as intended. Fig. 29 shows the speed error for the MPC and FMPC with the NEDC and US06 drive cycles. Figs. 29a - 29d show that the errors converge to zero during the system operation. The absolute average error for the MPC is 1.17 and 1.19 while the absolute average error for the FMPC is 3.02 and 3.13 with the NEDC and US06 drive cycles respectively. Even though the FMPC errors converge to zero, it experiences a degradation in speed tracking performance as compared to the MPC speed regulator.

2) CURRENT CONSUMPTION

The torque regulating current signal i^*_{sq} is displayed in Fig. 30. Figs. 30a and 30b show the extent of the control effort imposed by the MPC to regulate the speed of the EV traction system with the NEDC and US06 drive cycles respectively. Whereas, Figs. 30c and 30d show the effect of taking $dSOC/dt$ and d^2SOC/dt^2 into account when producing the signal i^*_{sq} during the speed tracking process with the FMPC. The control effort applied by the FMPC is very minimal, as compared to the MPC, as it restricts the current drawn by the motor from the battery bank while regulating the motor speed. The $i^*_{sq\ avg}$ applied by the MPC is 1.0683 A and 1.1616 A, while that applied by the FMPC is 1.0512 A and 1.1363 A with the NEDC and US06 drive cycles respectively. Fig. 31 shows the input weight R produced by the FMPC with the NEDC and US06 drive cycles. As expected, the weights display a similar pattern to the drive cycle speed

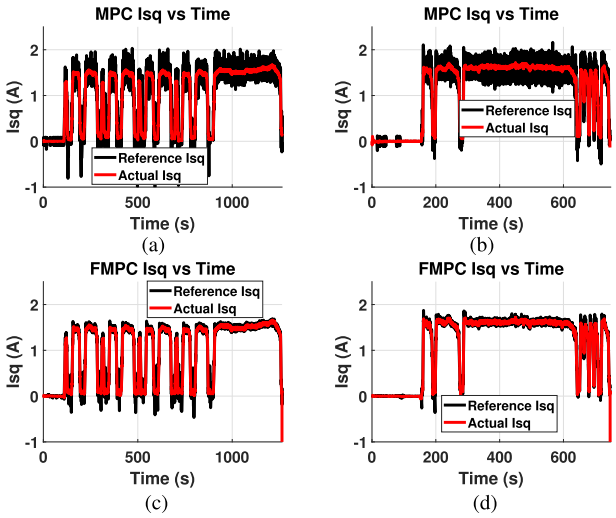

FIGURE 30. (a) MPC current i^*_{sq} with the NEDC drive cycle, (b) MPC current i^*_{sq} with the US06 drive cycle, (c) FMPC current i^*_{sq} with the NEDC drive cycle, (d) FMPC current i^*_{sq} with the US06 drive cycle.

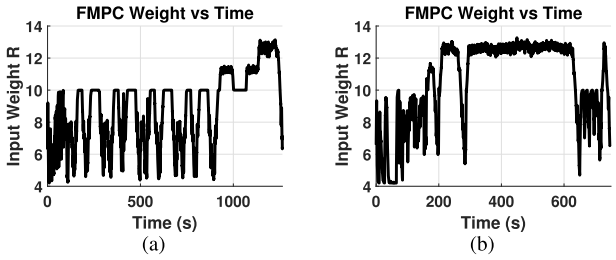

FIGURE 31. (a) FMPC input weight with the NEDC drive cycle, (b) FMPC input weight with the US06 drive cycle.

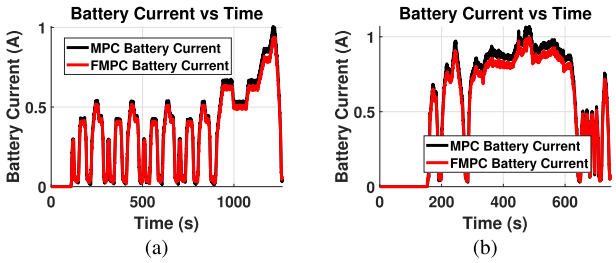

FIGURE 32. (a) Li-ion battery bank current profile of MPC and FMPC with the NEDC drive cycle, (b) Li-ion battery bank current profile of MPC and FMPC with the US06 drive cycle.

profile. When the speed increases, the $dSOC/dt$ increases which also increases the weight R. A larger R limits the i^*_{sq} variation and thus lowers the current drawn from the battery bank. Fig. 32 shows the battery bank current over the duration of the NEDC and US06 drive cycles. Figs. 32a and 32b show that the MPC consistently consumes a higher current than the FMPC with the NEDC and US06 drive cycles. Furthermore, Fig. 32a shows that the battery current gap between the MPC controller and FMPC widens during the extra-urban stage [900, 1260] seconds of the drive cycle. The same effect can be seen in figure 32b with the US06 drive cycle during the

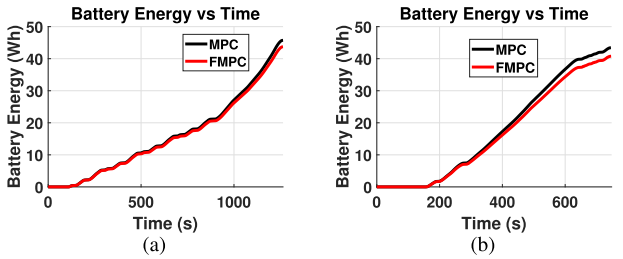

FIGURE 33. (a) MPC and FMPC battery energy consumption with the NEDC drive cycle, (b) MPC and FMPC battery energy consumption with the US06 drive cycle.

highway section [300, 600] seconds. This is attributed to the constant input weight R placed on the torque regulating current command i^*_{sq} during the speed regulation process. The battery current consumed by the MPC spans from [0, 1.02] A and [0, 1.08] A, while it spans from [0, 0.94] A and [0, 1] A for the FMPC with the NEDC and US06 drive cycles respectively. Furthermore, the mean value of the battery current $i_{bat\ avg}$ occurs at 0.33455 A and 0.5575 A for the MPC, while $i_{bat\ avg}$ occurs at 0.3305 A and 0.5228 A for the FMPC with the NEDC and the US06 drive cycles respectively. In other words, the FMPC consumes an overall lower average battery current with both drive cycles as compared to MPC.

3) BATTERY BANK ENERGY, SOC, SOH, RUNTIME AND LIFETIME MEASUREMENTS

Fig. 33 shows the energy consumed from the battery by the EV traction system with the NEDC and US06 drive cycles. The MPC consumed 45.72 Wh and 43.41 Wh, whereas the FMPC consumed 43.72 Wh and 40.76 Wh yielding an improvement of 4.4% and 6.1% with the NEDC and US06 drive cycles respectively. Figs. 34 and 35 show the change in SOC and SOH over the course of the NEDC and US06 drive cycles. The MPC shows a larger degradation than the FMPC in both SOC and SOH with both drive cycles. The final value of the SOC for the MPC is 0.9697 and 0.9711 yielding an SOC consumption of 0.0303 and 0.0289, while the FMPC changed the SOC value to 0.9710 and 0.973 yielding an SOC consumption of 0.029 and 0.027 with the NEDC and US06 drive cycles respectively. The FMPC has reduced the SOC consumption by 4.3% and 6.6% over the duration of the NEDC and US06 drive cycles. Furthermore, the final value of the SOH for the MPC is 0.99991624 and 0.9999202 yielding an SOH degradation of 0.00008376 and 0.0000798, while the FMPC final SOH values were 0.99991985 and 0.999925 yielding an SOH degradation of 0.00008015 and 0.000075 with the NEDC and US06 drive cycles respectively. The FMPC has reduced the SOH degradation by 4.3% and 6.0% with the NEDC and US06 drive cycles.

The estimated runtime for the MPC was 7.907 hours and 4.205 hours, while for the FMPC it was 8.256 hours and 4.492 hours with the NEDC and US06 drive cycles respectively. Therefore, there was an increase in runtime by

TABLE 8. Summary of the experimental results for MPC and FMPC.

Measurements \ Controllers	NEDC			US06		
	MPC	FMPC	Savings	MPC	FMPC	Savings
Absolute Average Error (RPM)	**1.17**	3.02	-	**1.19**	3.13	-
Control Effort $i^*_{sq\ avg}$ (A)	1.0683	**1.0512**	-	1.1616	**1.1363**	-
Battery Current $i_{bat\ avg}$ (A)	0.3455	**0.3305**	-	0.5575	**0.5228**	-
Final SOC (%)	96.97	**97.10**	4.3%	97.11	**97.30**	6.6%
Final SOH	0.99991624	**0.99991985**	4.3%	0.9999202	**0.999925**	6.0%
Battery Energy (Wh)	45.72	**43.72**	4.4%	43.41	**40.76**	6.1%
Estimated Runtime (hours)	7.907	**8.256**	4.4%	4.205	**4.492**	6.8%
Estimated Lifetime (hours)	74886	**78045.5**	4.2%	36921.5	**39766.6**	7.7%

The bold values indicate the best value (maximum or minimum).

0.349 hours (20 minutes 56 seconds) and 0.287 hours (17 minutes 13 seconds); in other words, 4.4% and 6.8% improvement in runtime. Furthermore, the estimate of the EOL for the MPC is 74886 hours and 36921.5 hours, whereas the estimate of the EOL for the FMPC occurs after 78045.5 hours and 39766.6 hours with the NEDC and US06 drive cycles respectively. The FMPC resulted in an increase of 3159.5 hours and 2845.1 hours corresponding to a 4.2% and 7.7% increase in battery lifetime over the course of the NEDC and US06 drive cycles respectively.

The graphical presentation demonstrates that the high fluctuations in motor current in Figs. 30a and 30b were reduced as shown in Figs. 30c and 30d. The FMPC managed to limit the motor current fluctuations which led to a lower consumption in battery current. Consequently, less battery energy was consumed. The input weight R in Fig. 31 adjusts to changes in battery $dSOC/dt$. When the motor draws a high i^*_{sq} current, the battery bank current consumption increases which also increases $dSOC/dt$. Therefore, the input weight R increases to limit both the i^*_{sq} variation and the current drawn from the battery bank. Figs. 32a and 32b show that the battery current consumed by the FMPC technique was lower than the battery current consumed by the MPC with the NEDC and US06 drive cycles respectively. Due to this reduction in battery current consumption, the battery energy, SOC, and SOH consumption were also reduced as shown in Figs. 33, 34, and 35 respectively. Figs. 33a and 33b, 34a and 34b,and 35a and 35b show that the FMPC reduced the battery energy, SOC, and SOH degradation as compared to the conventional MPC with the NEDC and US06 drive cycles respectively. Since the FMPC technique consumes less energy, SOC, and SOH from the battery bank, we conclude that the FMPC BEM strategy adds energy saving capability to IM drive and ultimately extends the battery bank runtime and lifetime. Table 8 summarizes all the obtained results for both the NEDC and US06 drive cycles.

C. CSFLC AND FMPC BATTERY ENERGY MANAGEMENT TECHNIQUES

The experimental evidence proves that the application of CSFLC and FMPC BEM techniques result in a significant

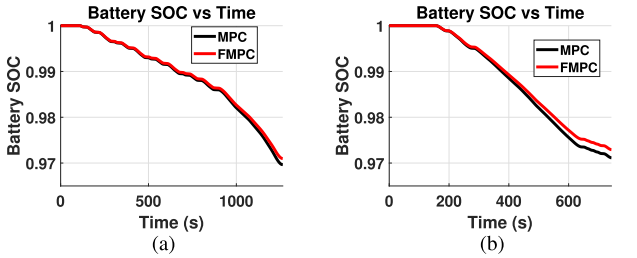

FIGURE 34. (a) SOC variation of the Li-ion battery bank with the NEDC drive cycle for MPC and FMPC, (b) SOC variation of the Li-ion battery bank with the US06 drive cycle for MPC and FMPC.

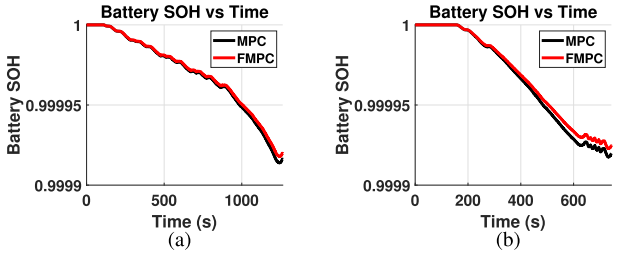

FIGURE 35. (a) SOH variation of the Li-ion battery bank with the NEDC drive cycle for MPC and FMPC, (b) SOH variation of the Li-ion battery bank with the US06 drive cycle for MPC and FMPC.

reduction in battery energy, SOC, and SOH degradation. However, the aforementioned improvements do not come at the same computational cost and degradation in motor speed tracking performance. The average savings per absolute average error in motor speed tracking is obtained and a comparison is made between the CSFLC and FMPC BEM techniques. Table 9 summarizes the absolute average errors and the percentage savings in battery energy, SOC, and SOH obtained from Tables 7 and 8. The percentage savings in Table 9 are divided by the corresponding absolute average error and the resultant percentage savings per absolute average error are displayed in Table 10.

Table 10 shows that with the NEDC drive cycle, the CSFLC (abbreviated α) results in higher percentage savings per absolute average error as compared to the FMPC (abbreviated μ). On the other hand, with the US06 drive

TABLE 9. Summary of the absolute average errors and percentage savings in drive cycle energy, SOC, and SOH for the CSFLC and the FMPC with the NEDC and US06 drive cycles.

	NEDC		US06	
Controllers / Measurements	CSFLC	FMPC	CSFLC	FMPC
Absolute Average Error (RPM)	3.7	**3.02**	6.93	**3.13**
Battery Energy	**8.2%**	4.4%	5.4%	**6.1%**
Battery SOC	**8.1%**	4.3%	5.9%	**6.6%**
Battery SOH	**8.3%**	4.3%	**6.4%**	6.0%

The bold values indicate the best value (maximum or minimum).

TABLE 10. Percentage savings in drive cycle energy, SOC, and SOH per absolute average error for the CSFLC and the FMPC with the NEDC and US06 drive cycles.

	NEDC		US06			
Controller/BEM technique / Percentage savings per absolute average error	CSFLC (α)	FMPC (μ)	CSFLC (β)	FMPC (Ω)	Average savings per absolute average error CSFLC $(\frac{\alpha+\beta}{2})$	Average savings per absolute average error FMPC $(\frac{\mu+\Omega}{2})$
Battery Energy	**2.21**	1.46	0.77	**1.95**	1.49	**1.70**
Battery SOC	**2.18**	1.42	0.84	**2.10**	1.51	**1.76**
Battery SOH	**2.24**	1.42	0.92	**1.92**	1.58	**1.67**

The bold values indicate the best value (maximum or minimum).

cycle, the CSFLC (abbreviated β) performance deteriorates significantly as compared to the FMPC (abbreviated Ω). The last two columns display an average of the CSFLC percentage savings per absolute average error $(\frac{\alpha+\beta}{2})$ with the NEDC and US06 drive cycles and the FMPC $(\frac{\mu+\Omega}{2})$ with the NEDC and US06 drive cycles. On average, the FMPC provides a higher average savings per absolute average error in battery energy consumption, SOC reduction, and SOH degradation as compared to the CSFLC. Furthermore, the controllers were compared based on their computational effort. The system was operated on a double timer scheme as described by the procedure in [38]. A sampling time of 100 μs was set for the IM drive system operation and a larger sampling time was set for the proposed controllers. The reason why a double timer scheme was adopted instead of a single timer scheme is that the performance of the IM drive system degrades when the sampling time increases [38]. Therefore, the computationally intensive part of the system is separately run with a larger sampling time, while the rest of the system is run with a smaller sampling time. That aside, the proposed strategies with a large computational time can be executed with a shorter sampling time if they had been implemented with a processor that has larger processing capabilities than dSPACE 1103. However, this will increase the cost of the IM drive hardware setup. The execution and sampling times are presented in Table 11. The MPC and FLC speed regulator without any energy management have smaller execution time. The proposed FMPC technique has a slightly larger execution time than the FLC. Finally, the CSFLC displayed the largest execution time. The sampling times are selected such that they are slightly higher than the execution time. To sum up, the FMPC BEM technique is superior to the CSFLC BEM technique due to its lower computational cost and higher average savings per absolute average speed error.

TABLE 11. Comparison between the sampling and execution times for the controllers.

Controller	Execution time	Sampling time
MPC	129 μs	200 μs
FLC	720 μs	800 μs
Proposed FMPC	780 μs	800 μs
Proposed CSFLC	1490 μs	1500 μs

V. CONCLUSION

This work designed and demonstrated the effectiveness of the proposed CSFLC and FMPC battery energy management techniques on an EV traction system. The objectives of battery bank SOC conservation, and lesser SOH degradation while estimating battery runtime and lifetime with the NEDC and US06 drive cycles are achieved. The experimental results showed that for the NEDC drive cycle, the CSFLC savings in energy, SOC, and SOH are 8.2%, 8.1% and 8.3% which extends the battery bank runtime and lifetime by 0.649 and 3917 hours respectively. The CSFLC BEM technique has a slight compromise on the motor speed error, the average speed error with the proposed BEM technique is 3.70 RPM

while using FLC without any BEM technique it is 1.28 RPM. Similarly, the FMPC savings for NEDC drive cycle are 4.4%, 4.3% and 4.3% with a battery runtime and lifetime elongation of 0.349 and 3159.5 hours respectively, and an average speed error of 3.02 RPM as compared to 1.17 RPM when MPC is employed without any BEM technique. Regarding the US06 drive cycle, the CSFLC savings are 5.4%, 5.9% and 6.4% with the battery bank runtime and lifetime elongation of 0.212 and 2145 hours for an average speed error of 6.93 RPM, as compared to 1.69 RPM for the FLC without employing the BEM technique. Likewise, the FMPC savings are 6.1%, 6.6% and 6.0% with a runtime and lifetime elongation of 0.287 and 2845 hours, and an average speed error of 3.13 RPM, as compared to 1.19 RPM for the MPC without using the proposed energy management technique. These improvements for the two drive cycles validated the effectiveness of CSFLC and FMPC in reducing the battery energy consumption, SOC, and SOH degradation, thus extending the battery bank runtime and lifetime with a minor loss in the speed tracking performance. Furthermore, the FMPC technique is superior to the CSFLC technique due to its higher average energy saving and lower computational effort. We conclude that the proposed CSFLC and FMPC battery energy management techniques not only increase the electric vehicle driving range, but also enhances the battery bank life with a minor compromise in the speed tracking performance.

Outlook and challenges:

1) The MPC can be updated to optimize the flux control by adjusting the i_{sd}^{*} for IM drive power efficiency. In addition, field weakening can be the topic of future work.
2) The CSFLC can have several other inputs influencing the scaling process. The SOH, increase in battery temperature and peak battery power can take part in the CSFLC decision making when scaling the motor current.

The following are the work limitations:

1) The MPC/FMPC performance is dependent upon the accuracy of the IM drive model. Therefore, the IM drive model must be updated online to achieve the best speed performance.
2) The CSFLC BEM technique is computationally intensive and very tedious to tune. Furthermore, it requires repetitive iterations to improve its performance. In future work, it is recommended to use a processor with higher capabilities than dSPACE 1103.
3) The BEM techniques in this paper can be incorporated in an actual EV which will help in battery energy conservation and extend the EV driving range. This is an open problem for today's EVs.

DISCLAIMER

This paper represents the opinions of the author(s) and does not mean to represent the position or opinions of the American University of Sharjah.

REFERENCES

[1] H. S. Ramadan, M. Becherif, and F. Claude, "Energy management improvement of hybrid electric vehicles via combined GPS/rule-based methodology," *IEEE Trans. Autom. Sci. Eng.*, vol. 14, no. 2, pp. 586–597, Apr. 2017.

[2] J. V. Barreras, C. Pinto, R. de Castro, E. Schaltz, S. J. Andreasen, P. O. Rasmussen, and R. E. Araujo, "Evaluation of a novel BEV concept based on fixed and swappable Li-ion battery packs," *IEEE Trans. Ind. Appl.*, vol. 52, no. 6, pp. 5073–5085, Nov. 2016.

[3] S. Recoskie, A. Fahim, W. Gueaieb, and E. Lanteigne, "Hybrid power plant design for a long-range dirigible UAV," *IEEE/ASME Trans. Mechatronics*, vol. 19, no. 2, pp. 606–614, Apr. 2014.

[4] A. F. Burke, "Batteries and ultracapacitors for electric, hybrid, and fuel cell vehicles," *Proc. IEEE*, vol. 95, no. 4, pp. 806–820, Apr. 2007.

[5] J. Shen and A. Khaligh, "Design and real-time controller implementation for a battery-ultracapacitor hybrid energy storage system," *IEEE Trans. Ind. Informat.*, vol. 12, no. 5, pp. 1910–1918, Oct. 2016.

[6] L. Zhang, X. Hu, Z. Wang, F. Sun, J. Deng, and D. G. Dorrell, "Multiobjective optimal sizing of hybrid energy storage system for electric vehicles," *IEEE Trans. Veh. Technol.*, vol. 67, no. 2, pp. 1027–1035, Feb. 2018.

[7] J. Wu, J. Ruan, N. Zhang, and P. D. Walker, "An optimized real-time energy management strategy for the power-split hybrid electric vehicles," *IEEE Trans. Control Syst. Technol.*, vol. 27, no. 3, pp. 1194–1202, May 2018.

[8] Y. Liu, J. Li, Z. Lei, W. Li, D. Qin, and Z. Chen, "An adaptive equivalent consumption minimization strategy for plug-in hybrid electric vehicles based on energy balance principle," *IEEE Access*, vol. 7, pp. 67589–67601, 2019.

[9] D. Q. Mayne, J. B. Rawlings, C. V. Rao, and P. O. M. Scokaert, "Constrained model predictive control: Stability and optimality," *Automatica*, vol. 36, no. 6, pp. 789–814, 2000.

[10] M. B. Shadmand, R. S. Balog, and H. Abu-Rub, "Model predictive control of PV sources in a smart DC distribution system: Maximum power point tracking and droop control," *IEEE Trans. Energy Convers.*, vol. 29, no. 4, pp. 913–921, Dec. 2014.

[11] S. Dusmez and A. Khaligh, "A supervisory power-splitting approach for a new ultracapacitor–battery vehicle deploying two propulsion machines," *IEEE Trans. Ind. Informat.*, vol. 10, no. 3, pp. 1960–1971, Aug. 2014.

[12] S. G. Li, S. M. Sharkh, F. C. Walsh, and C. N. Zhang, "Energy and battery management of a plug-in series hybrid electric vehicle using fuzzy logic," *IEEE Trans. Veh. Technol.*, vol. 60, no. 8, pp. 3571–3585, Oct. 2011.

[13] J. P. F. Trovao, M.-A. Roux, E. Menard, and M. R. Dubois, "Energy- and power-split management of dual energy storage system for a three-wheel electric vehicle," *IEEE Trans. Veh. Technol.*, vol. 66, no. 7, pp. 5540–5550, Jul. 2017.

[14] T. Sadeq, C. K. Wai, E. Morris, Q. A. Tarboosh, and O. Aydogdu, "Optimal control strategy to maximize the performance of hybrid energy storage system for electric vehicle considering topography information," *IEEE Access*, vol. 8, pp. 216994–217007, 2020.

[15] M. H. Hajimiri and F. R. Salmasi, "A fuzzy energy management strategy for series hybrid electric vehicle with predictive control and durability extension of the battery," in *Proc. IEEE Conf. Electr. Hybrid Vehicles*, Dec. 2006, pp. 1–5.

[16] V. Galdi, A. Piccolo, and P. Siano, "A fuzzy based safe power management algorithm for energy storage systems in electric vehicles," in *Proc. IEEE Vehicle Power Propuls. Conf.*, Sep. 2006, pp. 1–6.

[17] D. Phan, A. Bab-Hadiashar, M. Fayyazi, R. Hoseinnezhad, R. N. Jazar, and H. Khayyam, "Interval type 2 fuzzy logic control for energy management of hybrid electric autonomous vehicles," *IEEE Trans. Intell. Vehicles*, vol. 6, no. 2, pp. 210–220, Jun. 2021.

[18] M. Suhail, I. Akhtar, S. Kirmani, and M. Jameel, "Development of progressive fuzzy logic and ANFIS control for energy management of plug-in hybrid electric vehicle," *IEEE Access*, vol. 9, pp. 62219–62231, 2021.

[19] Q. A. Tarbosh, O. Aydogdu, N. Farah, M. H. N. Talib, A. Salh, N. Cankaya, F. A. Omar, and A. Durdu, "Review and investigation of simplified rules fuzzy logic speed controller of high performance induction motor drives," *IEEE Access*, vol. 8, pp. 49377–49394, 2020.

[20] Z. Chen, C. C. Mi, J. Xu, X. Gong, and C. You, "Energy management for a power-split plug-in hybrid electric vehicle based on dynamic programming and neural networks," *IEEE Trans. Veh. Technol.*, vol. 63, no. 4, pp. 1567–1580, May 2014.

[21] S. Xie, J. Peng, and H. He, "Plug-in hybrid electric bus energy management based on stochastic model predictive control," *Energy Proc.*, vol. 105, pp. 2672–2677, May 2017.
[22] A. Rezaei, J. B. Burl, B. Zhou, and M. Rezaei, "A new real-time optimal energy management strategy for parallel hybrid electric vehicles," *IEEE Trans. Control Syst. Technol.*, vol. 27, no. 2, pp. 830–837, Mar. 2019.
[23] H.-Q. Guo, C.-Z. Liu, J.-W. Yong, X.-Q. Cheng, and F. Muhammad, "Model predictive iterative learning control for energy management of plug-in hybrid electric vehicle," *IEEE Access*, vol. 7, pp. 71323–71334, 2019.
[24] Y. Zhang, L. Chu, Y. Ding, N. Xu, C. Guo, Z. Fu, L. Xu, X. Tang, and Y. Liu, "A hierarchical energy management strategy based on model predictive control for plug-in hybrid electric vehicles," *IEEE Access*, vol. 7, pp. 81612–81629, 2019.
[25] H. Chen, R. Xiong, C. Lin, and W. X. Shen, "Model predictive control based real-time energy management for hybrid energy storage system," *CSEE J. Power Energy Syst.*, vol. 7, no. 4, pp. 862–874, Jul. 2021.
[26] M. A. S. Kamal, M. Mukai, J. Murata, and T. Kawabe, "Ecological vehicle control on roads with up-down slopes," *IEEE Trans. Intell. Transp. Syst.*, vol. 12, no. 3, pp. 783–794, Sep. 2011.
[27] J. Guo, H. He, and C. Sun, "ARIMA-based road gradient and vehicle velocity prediction for hybrid electric vehicle energy management," *IEEE Trans. Veh. Technol.*, vol. 68, no. 6, pp. 5309–5320, Aug. 2019.
[28] C. Zhang, A. Vahidi, P. Pisu, X. Li, and K. Tennant, "Role of terrain preview in energy management of hybrid electric vehicles," *IEEE Trans. Veh. Technol.*, vol. 59, no. 3, pp. 1139–1147, Mar. 2010.
[29] G. Jinquan, H. Hongwen, P. Jiankun, and Z. Nana, "A novel MPC-based adaptive energy management strategy in plug-in hybrid electric vehicles," *Energy*, vol. 175, pp. 378–392, May 2019.
[30] S. Zhang, Y. Luo, J. Wang, X. Wang, and K. Li, "Predictive energy management strategy for fully electric vehicles based on preceding vehicle movement," *IEEE Trans. Intell. Transp. Syst.*, vol. 18, no. 11, pp. 3049–3060, Nov. 2017.
[31] J. Kim, H. Kim, J. Bae, D. Kim, J. S. Eo, and K.-K.-K. Kim, "Economic nonlinear predictive control for real-time optimal energy management of parallel hybrid electric vehicles," *IEEE Access*, vol. 8, pp. 177896–177920, 2020.
[32] C. Zhai, F. Luo, and Y. Liu, "A novel predictive energy management strategy for electric vehicles based on velocity prediction," *IEEE Trans. Veh. Technol.*, vol. 69, no. 11, pp. 12559–12569, Sep. 2020.
[33] T. Ghandriz, B. Jacobson, N. Murgovski, P. Nilsson, and L. Laine, "Real-time predictive energy management of hybrid electric heavy vehicles by sequential programming," *IEEE Trans. Veh. Technol.*, vol. 70, no. 5, pp. 4113–4128, Mar. 2021.
[34] A. A. Malikopoulos, "Supervisory power management control algorithms for hybrid electric vehicles: A survey," *IEEE Trans. Intell. Transp. Syst.*, vol. 15, no. 5, pp. 1869–1885, Oct. 2014.
[35] A. Mohammadi, H. Asadi, S. Mohamed, K. Nelson, and S. Nahavandi, "Multiobjective and interactive genetic algorithms for weight tuning of a model predictive control-based motion cueing algorithm," *IEEE Trans. Cybern.*, vol. 49, no. 9, pp. 3471–3481, Sep. 2019.
[36] H. Mahmoudi, M. Aleenejad, P. Moamaei, and R. Ahmadi, "Fuzzy adjustment of weighting factor in model predictive control of permanent magnet synchronous machines using current membership functions," in *Proc. IEEE Power Energy Conf. Illinois (PECI)*, Feb. 2016, pp. 1–5.
[37] N. Farah, M. H. N. Talib, N. S. M. Shah, Q. Abdullah, Z. Ibrahim, J. B. M. Lazi, and A. Jidin, "A novel self-tuning fuzzy logic controller based induction motor drive system: An experimental approach," *IEEE Access*, vol. 7, pp. 68172–68184, 2019.
[38] N. Farah, M. H. N. Talib, Z. Ibrahim, Q. Abdullah, O. Aydogdu, M. Azri, J. B. M. Lazi, and Z. M. Isa, "Investigation of the computational burden effects of self-tuning fuzzy logic speed controller of induction motor drives with different rules sizes," *IEEE Access*, vol. 9, pp. 155443–155456, 2021.
[39] N. Mohan, *Advanced Electric Drives: Analysis, Control, and Modeling Using MATLAB/SIMULINK*. Hoboken, NJ, USA: Wiley, 2014.
[40] N. Jabbour and C. Mademlis, "Online parameters estimation and autotuning of a discrete-time model predictive speed controller for induction motor drives," *IEEE Trans. Power Electron.*, vol. 34, no. 2, pp. 1548–1559, Feb. 2018.
[41] A. S. A. Abdelaziz, H.-U. Rehman, and S. Mukhopadhyay, "Cascaded fuzzy controller for electric vehicle traction system battery energy management," in *Proc. Int. Aegean Conf. Electr. Mach. Power Electron. (ACEMP) Int. Conf. Optim. Electr. Electron. Equip. (OPTIM)*, Aug. 2019, pp. 366–371.
[42] H. Usman, S. Mukhopadhyay, and H. Rehman, "Performance enhancement of electric vehicle traction system using FO-PI controller," *IET Elect. Syst. Transp.*, vol. 9, no. 4, pp. 206–214, 2019.
[43] D. Ali, S. Mukhopadhyay, H. Rehman, and A. Khurram, "UAS based Li-ion battery model parameters estimation," *Control Eng. Pract.*, vol. 66, pp. 126–145, Mar. 2017.
[44] M. Chen and G. A. Rincon-Mora, "Accurate electrical battery model capable of predicting runtime and I–V performance," *IEEE Trans. Energy Convers.*, vol. 21, no. 2, pp. 504–511, Jun. 2006.
[45] H. M. Usman, S. Mukhopadhyay, and H. Rehman, "Universal adaptive stabilizer based optimization for Li-ion battery model parameters estimation: An experimental study," *IEEE Access*, vol. 6, pp. 49546–49562, 2018.
[46] D. N. How, M. A. Hannan, M. H. Lipu, and P. J. Ker, "State of charge estimation for lithium-ion batteries using model-based and data-driven methods: A review," *IEEE Access*, vol. 7, pp. 136116–136136, 2019.
[47] S. Ebbesen, P. Elbert, and L. Guzzella, "Battery state-of-health perceptive energy management for hybrid electric vehicles," *IEEE Trans. Veh. Technol.*, vol. 61, no. 7, pp. 2893–2900, Sep. 2012.
[48] H. M. Usman, H. Rehman, and S. Mukhopadhyay, "Electric vehicle traction system performance enhancement using FO-PI controller," in *Proc. IEEE Vehicle Power Propuls. Conf. (VPPC)*, Aug. 2018, pp. 1–5.
[49] D. Zhao, R. Stobart, G. Dong, and E. Winward, "Real-time energy management for diesel heavy duty hybrid electric vehicles," *IEEE Trans. Control Syst. Technol.*, vol. 23, no. 3, pp. 829–841, May 2015.
[50] Z. Yu, R. Huai, and L. Xiao, "State-of-charge estimation for lithium-ion batteries using a Kalman filter based on local linearization," *Energies*, vol. 8, no. 8, pp. 7854–7873, Jul. 2015.
[51] Q. Yang, J. Xu, B. Cao, D. Xu, X. Li, and B. Wang, "State-of-health estimation of lithium-ion battery based on interval capacity," *Energy Proc.*, vol. 105, pp. 2342–2347, May 2017.
[52] W. Lu, L. Zhang, Y. Qin, and A. Jansen, "Calendar and cycle life of lithium-ion batteries containing silicon monoxide anode," *J. Electrochemical Soc.*, vol. 165, no. 10, pp. A2179–A2183, 2018.
[53] J. Wang, P. Liu, J. Hicks-Garner, E. Sherman, S. Soukiazian, M. Verbrugge, H. Tataria, J. Musser, and P. Finamore, "Cycle-life model for graphite-$LiFePO_4$ cells," *J. Power Sources*, vol. 196, no. 8, pp. 3942–3948, Apr. 2011.
[54] S. Ebbesen, P. Elbert, and L. Guzzella, "Battery state-of-health perceptive energy management for hybrid electric vehicles," *IEEE Trans. Veh. Technol.*, vol. 61, no. 7, pp. 2893–2900, Sep. 2012.
[55] P. Ananto, F. Syabani, W. D. Indra, O. Wahyunggoro, and A. I. Cahyadi, "The state of health of Li-Po batteries based on the battery's parameters and a fuzzy logic system," in *Proc. Joint Int. Conf. Rural Inf. Commun. Technol. Electr.-Vehicle Technol. (rICT & ICeV-T)*, Nov. 2013, pp. 1–4.
[56] H. Rehman and A. Khurram, "Fuzzy logic enhanced sensorless alternative energy vehicular drive system," in *Proc. IEEE Vehicle Power Propuls. Conf. (VPPC)*, Dec. 2017, pp. 1–5.

AHMED SAYED ABDELAAL received the M.Sc. degree in electrical engineering from the American University of Sharjah (AUS), United Arab Emirates (UAE), in 2019. From 2018 to 2019, he worked as a Research Assistant at the AUS. Currently, he is open and looking for Ph.D. opportunities. His research interests include EV powertrain development and automotive design, power electronics, and electric drives and control systems.

SHAYOK MUKHOPADHYAY (Member, IEEE) received the B.E. degree in electrical engineering from the College of Engineering Pune, Savitribai Phule Pune University (formerly known as the University of Pune), India, in 2006, the M.Sc. degree in electrical engineering from Utah State University, Logan, UT, USA, in 2009, and the Ph.D. degree in electrical engineering from the Georgia Institute of Technology, Atlanta, GA, USA, in 2014. He has been with the Department of Electrical Engineering, American University of Sharjah, United Arab Emirates (UAE), since 2014, where he is currently an Associate Professor. His research interests include control systems, nonlinear systems, computational methods, battery modeling and failure detection, and robotic path planning. He received the Award for the Best Presentation in the Nonlinear Systems III Session from the American Control Conference 2014. He was a part of five-person team that received the National Category of the AI and Robotics for Good Award for developing an in-pipe inspection robot at UAE in 2017.

HABIBUR REHMAN (Member, IEEE) received the B.Sc. degree in electrical engineering from the University of Engineering and Technology at Lahore, Lahore, Pakistan, in 1990, and the M.S. and Ph.D. degrees in electrical engineering from The Ohio State University, Columbus, OH, USA, in 1995 and 2001, respectively. He has a wide experience in the areas of power electronics and motor drives in both industry and academia. From 1998 to 1999, he was a Design Engineer with the Ecostar Electric Drive Systems and Ford Research Laboratory, where he was a member of the Electric, Hybrid, and Fuel Cell Vehicle Development Programs. From 2001 to 2006, he was an Assistant Professor with the Department of Electrical Engineering, United Arab Emirates (UAE) University, Al Ain, UAE. In 2006, he joined the Department of Electrical Engineering, American University of Sharjah, where he is currently working as a Professor. His research interests include power electronics and their application to power systems, adjustable-speed drives, and alternative energy vehicles. He was a recipient of the Best Teacher Award (2002–2003) from the College of Engineering, UAE University.